Progress in Photovoltaics: Research and Applications

WILEY

PROGRESS IN PHOTOVOLTAICS

RESEARCH ARTICLE OPEN ACCESS

Progress Toward Efficient Wide-Gap Cu (In,Ga)(S,Se)$_2$ Thin-Film Solar Cells

Setareh Zahedi-Azad[1] | Roland Scheer[1] | Dimitrios Hariskos[2] | Stefan Paetel[2] | Wolfram Hempel[2] | Wolfram Witte[2] | Hao Luo[3] | Oana Cojocaru-Mirédin[3] | Mary Blankenship[4] | Dirk Hauschild[4,5,6] | Victor van Maris[5,6] | Lothar Weinhardt[4,5,6] | Clemens Heske[4,5] | Thomas Unold[7] | José A. Márquez[7] | Jasmin Seeger[8] | Florian Wilhelmi[8] | Michael Hetterich[8,9] | Thomas Niesen[10] | Patrick Eraerds[10] | Thomas Dalibor[10] | Xiaowei Jin[11] | Reinhard Schneider[11] | Dagmar Gerthsen[11] | Di Wang[12] | Christian Kübel[12]

[1]Institute of Physics, Martin-Luther-Universität Halle-Wittenberg (MLU), Halle, Germany | [2]Zentrum für Sonnenenergie- und Wasserstoff-Forschung Baden-Württemberg (ZSW), Stuttgart, Germany | [3]Department of Sustainable Systems Engineering (INATECH), University of Freiburg, Freiburg im Breisgau, Germany | [4]Department of Chemistry and Biochemistry, University of Nevada, Las Vegas (UNLV), Las Vegas, Nevada, USA | [5]Institute for Photon Science and Synchrotron Radiation (IPS), Karlsruhe Institute of Technology (KIT), Eggenstein-Leopoldshafen, Germany | [6]Institute for Chemical Technology and Polymer Chemistry (ITCP), Karlsruhe Institute of Technology (KIT), Karlsruhe, Germany | [7]Helmholtz-Zentrum Berlin für Materialien und Energie GmbH, Berlin, Germany | [8]Institute of Applied Physics (APH), Karlsruhe Institute of Technology (KIT), Karlsruhe, Germany | [9]Light Technology Institute (LTI), KIT, Karlsruhe, Germany | [10]AVANCIS GmbH, München, Germany | [11]Laboratory for Electron Microscopy, Karlsruhe Institute of Technology (KIT), Karlsruhe, Germany | [12]Institute of Nanotechnology, Karlsruhe Institute of Technology (KIT), Eggenstein-Leopoldshafen, Germany

Correspondence: Roland Scheer (scheer@physik.uni-halle.de)

Received: 27 February 2025 | **Revised:** 26 June 2025 | **Accepted:** 11 November 2025

ABSTRACT

In this paper, wide-gap Cu (In,Ga)(S,Se)$_2$ thin-film solar cells are studied in view of their performance, limitations, and opportunities for further optimization. To this end, a wide variety of properties is investigated. This includes the role of gallium gradients, grain size effects, electronic properties, doping metastabilities, and minority carrier lifetime. Particular emphasis is placed on the impact of alkali atoms. A comparison of surface, interface, and grain boundary chemistry shows systematic atomic accumulation and depletion effects. This leads to electronic modifications in the grain boundary regions of the absorber. Heavy alkali treatments also influence the device properties, giving a clear boost of open-circuit voltage. By the combination of different experimental results, this positive open-circuit voltage effect has been explained in terms of reduction of interface recombination. The latter effects are discussed in view of a possible alkali–indium–selenium bond formation at the interface between the absorber and the buffer layer. The properties of a 14.2%-efficient Cu (In,Ga)Se$_2$-based device with [Ga]/([Ga]+[In])=0.8 and a wide optical band gap of 1.48 eV are investigated, also in view of further opportunities for improvement.

1 | Introduction

Wide band gap Cu (In,Ga)(S,Se)$_2$ (CIGSSe) is a promising thin-film absorber material for the top cell in tandem devices [1]. Also, for single-junction devices, a bulk band gap in the region of 1.4 eV would be advantageous in terms of module design and smaller temperature coefficients. However, the efficiencies of thin-film solar cells based on wide-gap CIGSSe are limited to date by a large open-circuit voltage (V_{oc}) deficit (here defined as $\Delta V_{oc}=E_g/q-V_{oc}$). While ΔV_{oc} exhibits a value as low as 0.36 in the current champion device with a [Ga]/([Ga]+[In]) ratio (GGI) in the range of 0.3 [2], ΔV_{oc} increases for larger GGI and can exceed 0.8 V for GGI=1 [1]. There are a variety of obstacles that impede a smaller V_{oc} deficit for large GGI devices:

1. The CIGSSe conduction band minimum at the absorber surface is found to shift upward when GGI is increased. This can lead to a cliff in the conduction band alignment (ΔE_c) at the heterojunction between the absorber and chemical-bath deposited CdS (CBD-CdS), as previously seen at the interface between CBD-CdS and Se-free CIGS [3] or CIGSe with GGI = 0.9 [4]; a cliff can lead to increased interface recombination [5, 6]. In contrast, narrow-gap CIGSSe devices have, over the years, reproducibly exhibited a nearly flat conduction band alignment at their front contact interfaces [7–14]. Larsson et al. showed that a $Zn_{1-x}Sn_xO_y$ buffer layer, optimized for pure $CuGaSe_2$ (CGSe, i.e., GGI = 1), can reduce the V_{oc} deficit to about 0.6 V, leading to a champion efficiency of 11.9% [15]. Pushing up the conduction band minimum exclusively at the back contact by aluminum alloying lead to 12.25% efficiency by Ishizuka et al. [16].
2. Due to spontaneous formation of copper vacancy (V_{Cu}) acceptor defects, majority carrier type inversion (p to n) at the junction and thus a hole barrier with its role to prevent interface recombination [17] may be limited to values of $E_{CBM}{}^{if}-E_F = 0.6–0.8$ eV [18, 19], where $E_{CBM}{}^{if}$ and E_F are the conduction band minimum at the interface and the Fermi energy, respectively.
3. The minority carrier lifetime (as interpreted from luminescence measurements) decreases with increasing GGI [1], suggesting an increasing bulk defect density. Indeed, even bulk-recombination-limited wide-gap CIGSe cells (with a KF treatment) still exhibited limited performance [20].
4. Due to limited chemical diffusion, high GGI films can become inhomogeneous with Cu_2Se precipitates [21], a problem that may be mitigated by high-temperature annealing [22]. Also, Cu-rich grain boundaries have been observed mainly to occur on high GGI films [21].
5. The positive role of heavy-alkali post-deposition treatments (PDT), nowadays being indispensable for high-efficiency low-GGI devices [23, 24], seem to be ineffective for GGI = 1 devices [25], possibly due to the lack of an alkali-Ga-Se-type environment at the absorber/buffer interface [26].

Other observations for high GGI materials and devices are (i) a fluctuation of the space charge region (SCR) width due to varying interface charge or window doping [27]. While the fluctuations are similar in GGI = 0.30 and GGI = 0.66 samples, their impact may be higher for high GGI due to the risk of interface recombination. (ii) A high Se overpressure during growth increases V_{oc} and J_{sc} [1, 28]. (iii) Silver alloying also increases the band gap but with a lower conduction band minimum (CBM) [29], which can alleviate interface recombination losses caused by the cliff-like ΔE_c. Moreover, Ag incorporation promotes grain growth, thereby reducing structural disorder [30]. However depending on group-I/III stoichiometry, high levels of Ag incorporation can negatively impact material stability and performance [31]. Since Ag addition has an impact on many material parameters, ACIGSe here is left out in order to focus on the high gallium effects.

In this paper, the results on high-GGI CIGSSe and Cu (In,Ga)Se_2 (CIGSe) materials and corresponding devices collected within the German joint research projects "EFFCIS" and "EFFCIS-II" are presented. The paper is organized as follows: After a summary of experimental details, the results and discussion sections present growth properties, interface aspects, electronic properties, and device aspects of wide-gap CIGSSe and CIGSe absorbers, including small-area cells and sub-modules.

2 | Methods

The CIGSe layers in this work were prepared via vacuum processes using three-stage (MLU [32]) or in-line evaporation (ZSW, NICE Solar [33]), while CIGSSe absorbers were prepared in a sequential preparation (AVANCIS [34]) with an overall Cu-poor stoichiometry. At MLU, heavy-alkali (HA) post-deposition treatments (PDT) of the CIGSe absorbers were performed in situ at 723 K under constant selenium flux by KF, RbF, or CsF evaporation, with rates of 0.01 nm/s for 600, 1925, and 800 s, respectively. We emphasize that the term "heavy alkali" here shall apply to all alkali elements beyond sodium. For the MLU devices, sodium supply came from the Guardian or Schott glass substrates unless stated otherwise in the text below. PDTs at ZSW were done with RbF in the in-line machine under a Se atmosphere without breaking the vacuum, while sodium supply was also realized by the glass substrate. PDTs at AVANCIS were carried out after the absorber formation by evaporation of a Na compound with subsequent annealing in vacuum. The CIGSe absorbers were completed to solar cells using the stacking sequence (from bottom to top) glass/sputtered Mo/CIGSe/buffer layer/sputtered i-ZnO/emitter ZnO:Al or In_2O_3:SnO_2 (ITO). The CdS buffer layers were deposited by chemical bath deposition either 15–30 min after CIGS deposition (ZSW, Nice) or within hours (MLU). Industrial devices from AVANCIS received a sputtered Zn(O,S) buffer layer directly after CIGSSe fabrication (AVANCIS). Laboratory cells received a Ni/Al grid and were defined by mechanical scribing to an area of 0.5 cm^2. CIGSe modules were obtained by monolithic interconnection [35]. In this manuscript, buffer/absorber interfaces are either denoted as "absorber/buffer" (i.e., following the p/n junction convention) or "buffer/absorber" (i.e., following the conventions in the surface/interface science community), depending on context.

Glow-discharge-optical-emission-spectroscopy (GDOES) profiles were recorded and compared with a variety of elemental and compound standards. For simplicity, the GDOES profiles were plotted versus a linearly averaged calculated depth, obtained from $t_{sputter} \times z_{max}/t_{max}$, where $t_{sputter}$ is the sputtering time for a given data point, z_{max} is the maximum thickness as determined by profilometry, and t_{max} is the time needed to reach z_{max}. Kelvin probe force microscopy (KPFM) was performed on cleaved cross-sections of solar cells, with an additional gold layer prepared as described in Ref. [36].

Cross-sectional specimens for transmission electron microscopy (TEM) were prepared by focused ion beam (FIB) milling using an FEI Helios G4 dual-beam microscope. The FIB lamellae were attached to Si (Cu-free) lift-out grids to avoid stray X-rays from Cu. They were polished by a Ga^+-ion beam with a low energy of 1 keV to minimize Ga^+ implantation and material amorphization. The crystal structure and microchemistry of the CIGSe/CdS interfacial regions were investigated by combined high-angle annular dark-field (HAADF) imaging in scanning transmission electron microscopy (STEM) and energy-dispersive

X-ray spectroscopy (EDXS) at 300 kV primary electron energy with a probe-corrected ThermoFisher Themis 300 microscope.

Raman spectroscopy was performed on a Horiba LabRAM (HeNe-Laser (633 nm), 50× objective, measurement range from 125 to 700 cm^{-1}.

Atom probe tomography (APT) was employed to quantify the Ga and alkali redistribution in 3D and down to the nanometer level [37–40]. APT measurements were conducted on a local electrode atom probe (versions LEAP 4000 X Si and 5000 XS, Cameca, United States). Laser pulses with a wavelength of ~355 nm, a pulse duration of 10 ps, and an energy of 3–5 pJ were used. A pulse repetition rate of 250 kHz with a detection rate of 0.5% on average, an ion flight path of 110 to 160 mm, and a specimen base temperature of 40 K were utilized. The APT data were processed using a commercial software package (IVAS 3.8.0, Cameca instruments).

Solar-cell parameters were obtained at standard testing conditions using a simulated AM1.5G spectrum. All denoted efficiencies are total-area values for cells without anti-reflective coating (ARC), unless denoted otherwise. Thicknesses of absorber layers were determined with SEM or XRF. XRF and SEM–EDX were used to determine the chemical composition of CIGSe absorber layers. Temperature-dependent current–voltage JV(T) measurements were conducted in a cryostat with a closed helium cycle, in a temperature range between 100 and 300 K in 10 K steps. Illumination for JV(T) was provided by a xenon lamp from Science-tech with a calibrated AM1.5G spectrum. Due to the heat of the lamp, the minimum temperature that could be achieved with white-light illumination was 100 K. The activation energy of the saturation current (E_A) was estimated from temperature-dependent current–voltage JV(T) measurements in the temperature range of 283–318 K with 5-K intervals and a linear extrapolation of the high-temperature region to 0 K. For $V_{oc}(t)$ transients, the samples were first relaxed at 318 K for 16 h in a dark chamber at atmospheric pressure. After opening the light shutter, the samples were exposed to red light from an LED source at room temperature at an energy flux of 30 mW/cm^2. During illumination, the V_{oc} was measured in constant time intervals. The procedure to measure open-circuit transients, including temperature correction, has been described in Ref. [41]. The external quantum efficiency (EQE) was recorded with a monochromator under chopped illumination and using a lock-in technique with an additional white light bias (MLU: Newport-74,125; ZSW: BENTHAM PVE 300). The optical band gap was determined at the long-wavelength value of 20% normalized EQE and by the leading edge of an $(E*\mathrm{EQE})^2$ versus E plot. Admittance spectra to extract the capacitance density C as a function of frequency f ($C(f)$) were recorded at low temperatures (100 or 120 K) and frequencies between 10^3 and 10^6 Hz. An Agilent E4980A LCR-meter was used to record the capacitance spectra with an AC bias range of 0.05 V_{rms}. The procedure follows the one introduced by Obereigner et al. [6]. The doping density is calculated from the space charge region capacitance C_{scr}. The space charge capacitance C_{scr} is determined at the frequency f where the logarithmic derivative $-dC/d(\log f)$ has its minimum. In the relaxed state, we find for both RbF-treated and untreated samples with the GGI = 0.3, the C_{scr} at $f \sim 10^4$ Hz, and after illumination at $5*10^5$ and 10^5 Hz, respectively. For samples with the GGI = 0.75 in the relaxed state, the C_{scr} is determined at the frequency of ~103 Hz. After illumination, the C_{scr} is extracted at $f \sim 10^4$ and ~10^5 Hz for untreated and RbF-treated samples, respectively.

To study the chemical and electronic structure at the sample surfaces, x-ray photoelectron spectroscopy (XPS), ultraviolet photoelectron spectroscopy (UPS), and inverse photoemission spectroscopy (IPES) were employed [12]. For this purpose, a CIGSe sample series with three different GGIs (0.30, 0.66, and 0.95) and a CdS/CIGSe interface sample (GGI of 0.95) were shipped under N_2 atmosphere from ZSW to KIT. At KIT, the samples were unpacked in an Ar-filled glovebox and separated into two sets. The first set remained at KIT, and the second set was repacked under Ar and sent to UNLV. At KIT, the samples were measured with an Omicron Argus CU electron analyzer using a twin anode X-ray source (DAR450, Omicron) for non-monochromatized Mg and Al K_α, and a He gas discharge lamp (HIS 13 UV Source, Omicron) for He I and II excitation. At UNLV, XPS spectra were recorded with a Scienta R4000 electron analyzer and a monochromatized x-ray source (Scienta SAX-100). For UPS, a monochromatized Gammadata VUV 5000 photon source was used. For IPES, a STAIB low-energy electron source (NEK-150–1) and a Hamamatsu R6834 photomultiplier with a Semrock Hg01-254-25 mercury line filter were employed. All XPS energy axes were calibrated according to Ref. [42] using sputter-cleaned Au, Ag, and Cu foils. The Au and Ag foils were also used to calibrate the Fermi energy for UPS and IPES measurements.

Computer simulations of $V_{oc}(t)$ transients were performed by Synopsys TCAD using a one-dimensional model represented by a mathematical mesh, which is generated by Delaunay triangulation [43, 44] with a model for HA PDT-treated devices as in Ref. [45]. It is emphasized that Synopsys TCAD uses the Fermi-Dirac statistics, which allow for accurate results even at low temperatures.

3 | Growth Properties

In this section, the influences of composition gradients, sodium, and the growth temperature on the properties of wide-gap CIGSe are discussed. The use of small indium amounts in the wide-gap material is motivated by the possibility of forming a band gap gradient, which can support carrier collection and reduce recombination in the bulk and at the back contact. Further, indium atoms may allow forming HA-In-Se bonds at the surface.

3.1 | High GGI Can Lead to Strong Gradients

Due to the limited diffusion of Ga in Cu (In,Ga)Se_2 [46], sequential deposition protocols for CIGSe inherently can lead to gradients in the GGI ratio and resultant band gap profiles. This is particularly true for the three-stage evaporation process [47], where a double GGI gradient is formed, with a minimum ("notch") and GGI ratios increasing toward front and back contact. Figure 1a compares the GGI gradients of samples with a low integral GGI of 0.35 and a high integral GGI of 0.85 from the static three-stage evaporation process

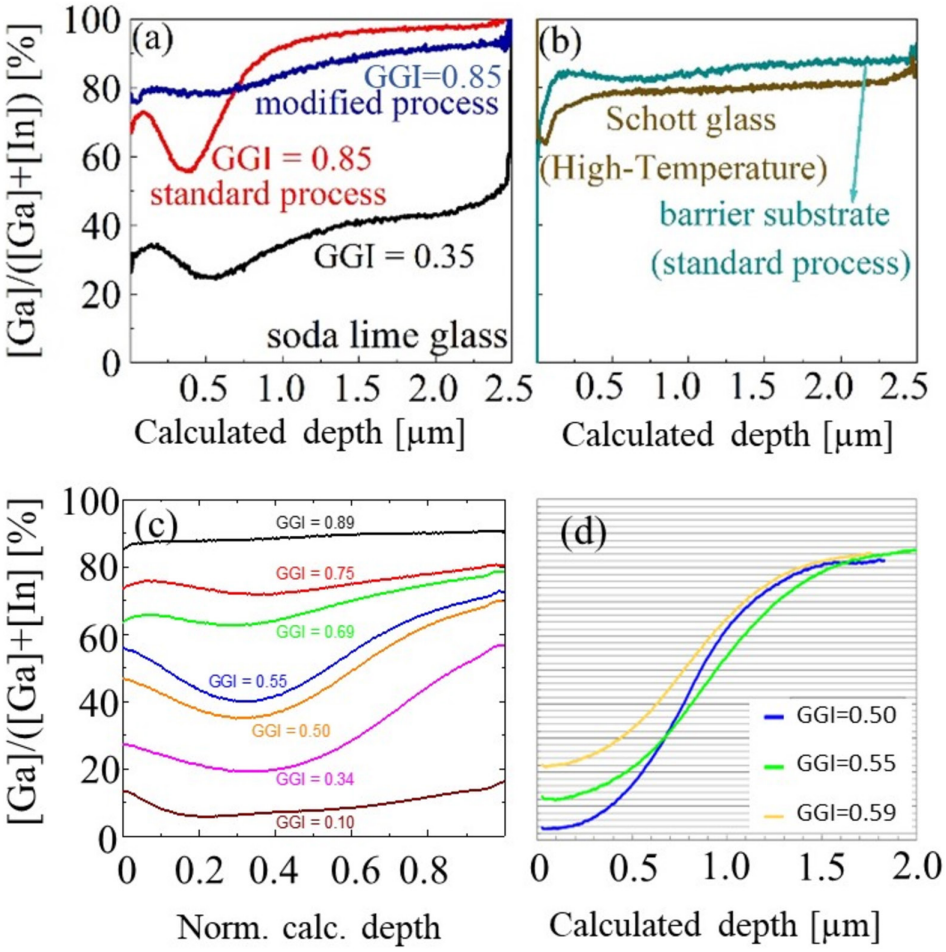

FIGURE 1 | GGI profiles of CIGSe and CIGSSe samples with different integral GGI as measured by GDOES (Mo back contact is on right side of each image). (a) CIGSe grown at MLU by a three-stage process [32, 45] at a nominal substrate temperature of 625°C and deposition time of 2300 s. In the modified process of GGI = 0.85, gallium was additionally deposited in the second stage. (b) CIGSe films obtained by high-temperature (675°C) growth at MLU on Schott glass as well as 625°C temperature growth on a barrier-coated substrate (i.e., without sodium). (c) CIGSe films from an in-line process of ZSW for different integral GGI absorbers. (d) Cu (In,Ga)$(Se,S)_2$ absorbers with different GGI prepared by the sequential process of AVANCIS.

at MLU. For the static three-stage process, high GGI samples develop steeper gradients at the same deposition conditions (substrate temperature and deposition time) than those with low GGI [32, 45]. Ref. [43] shows that a too steep GGI gradient toward the front surface can impede current collection in the solar cell. Indeed, Ref. [45] revealed an inferior fill factor and EQE red response for the regular static three-stage process shown in Figure 1a. In Ref. [47], it was suggested that the strong GGI gradient can be avoided by Ga deposition in the second stage of the three-stage process. The calculated depth profile for the modified process in Figure 1a confirms that this approach is also applicable to absorbers with a high integral GGI of 0.85. At standard substrate temperature and for Ga deposition in the second stage, the GGI gradient of the modified process is reduced. Another aspect is that gallium diffusion is inhibited by sodium doping but is promoted by a higher substrate temperature of 675°C. This is both visible in Figure 1b, where a less-pronounced GGI gradient is achieved by growth with an applied diffusion barrier underneath the molybdenum back contact or by growth at higher substrate temperature on high-temperature Schott glass. In contrast to the static three-stage process at MLU, CIGSe growth from the inline multi-stage process at ZSW on seven successive carriers seems to be producing less steep GGI gradients. This can be seen in Figure 1c, where the GGI gradient becomes less pronounced with larger integral GGI. Besides a somewhat higher substrate temperature, this may be due to the different growth schemes, with metal evaporation sources in two deposition chambers depositing onto the moving carriers. For example, in the second chamber, the second and third stages of the classical three-stage process are emulated, without any spatial separation, which might lead to a different layer formation behavior. To sum up Figure 1, it becomes visible that the GGI profile in high GGI absorbers can be tailored to form a gradient toward the back contact, such that it induces an effective force field for the collection of minority charge carriers. However, such a gradient may be diminished during high-temperature growth of CIGSe, due to enhanced interdiffusion between the absorber elements. The GGI profile produced by selenization/sulfurization of metal precursors (sequential process) at AVANCIS (a) reveals a pronounced band gap gradient toward the back contact. With increasing integral GGI from 0.50 to 0.59, this gradient becomes smaller by raising the front GGI while keeping the back gradient unaffected.

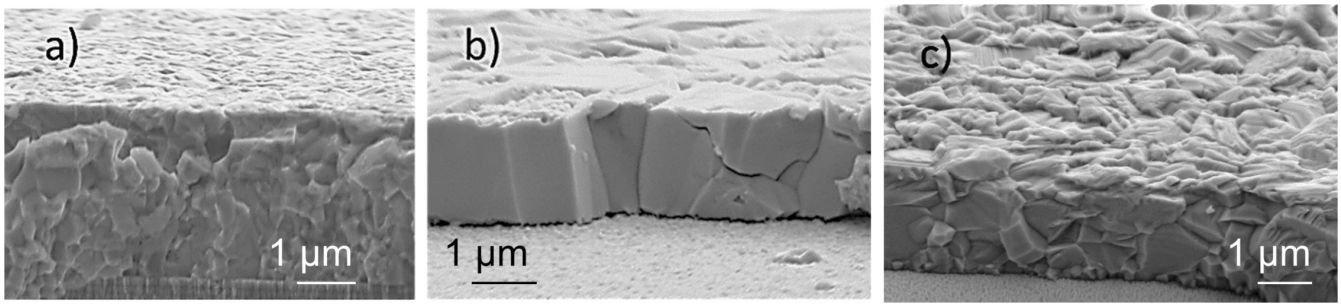

FIGURE 2 | SEM cross-sections of MLU Cu (In,Ga)Se_2 films with GGI = 0.8. (a) 625°C temperature growth on standard soda-lime glass. (b) High-temperature (675°C) growth on Schott high-temperature glass. (c) 625°C temperature growth on barrier glass. Markers indicate 1 µm.

3.2 | $CuS_{1-x}Se_x$ Secondary Phase Formation

Ref. [48] shows that (In-free) $CuGaSe_2$ growth can be accompanied by the remaining of Cu-Se bulk precipitates even in an integral Cu-poor film. Such Cu-binary phases might degenerate the majority carrier concentrations, leading to shunt paths in the devices [49]. Two samples from the sequential growth process of AVANCIS both with relatively high GGI of 0.55–0.59 were analyzed by Raman spectroscopy. Both samples show the two A_1 modes for Cu (In,Ga)Se_2 and Cu (In,Ga)S_2 at ~180 and ~300 cm^{-1}, respectively (see Figure S2). In addition, the GGI = 0.59 sample exhibits a Raman peak at 360 cm^{-1}, which can be related to a $CuS_{1-x}Se_x$ phase with a large x [50]. By reducing the sodium concentration, the $CuS_{1-x}Se_x$ phase amount could be reduced (see sample GGI = 0.55), but the solar cell efficiencies remained well below the possible values of GGI = 0.55 devices (Figure S2). This indicates that a small amount of $CuS_{1-x}Se_x$ is not the main source of the performance limitation of wide-gap CIGSSe.

An improved photovoltaic device performance was reported for wide-gap CIGSe when using higher substrate temperatures during growth [51] (in comparison with narrow-gap CIGSe). An explanation can possibly be found in the higher melting temperature of high GGI versus low GGI CIGSe.[1] For equal "distances" from the equilibrium between nucleation and melting, high GGI growth requires a higher temperature than low GGI growth. Also, the limited diffusion of Ga in CIGSe may require a higher temperature [46], although the literature is contradictory on this topic [53].

3.3 | Grain Size Can Be Increased

Besides influencing the GGI gradient, the high-temperature growth increases the grain size of the polycrystalline CIGSe absorber. This can clearly be seen in the cross-section SEM images of MLU absorbers in Figure 2b by comparing it with the 625°C temperature growth in Figure 2a. Grains of dimensions of the film thickness develop upon a high substrate temperature of 675°C. Besides the substrate temperature, the Na concentration also has an impact on the grain size. Figure 2c shows that the grain size increases at a standard 625°C temperature for high GGI samples if the film is grown on barrier-coated glass without Na [45]. The Na content in the high-temperature sample is also lower, possibly due to lower Na concentration in the Schott glass. Therefore, it is suggested that larger grain sizes (such as in Figure 2b) can be achieved at high temperatures and/or low Na content.

4 | Bulk Electronic Properties

In this section, we focus on bulk properties, such as doping concentration and metastabilities, as well as on the minority carrier lifetimes in wide-gap versus narrow-gap CIGSe.

4.1 | Heavy-Alkali PDTs Increase Doping Metastability

It has frequently been reported that CIGSe layers exhibit a metastable doping that increases upon illumination [6, 41, 54, 55]. The general effect can be seen in Figure 3, which shows the doping levels after different illumination times as derived from admittance spectra as in Figure S1: The untreated 0.30 and 0.75 GGI MLU samples (red curves) exhibit an increase in the apparent acceptor concentration $N_{A,a}(t)$ as a function of red-light illumination time (wavelength > 630 nm, "red-light soaking"). As in Ref. [6], the $N_{A,a}(t)$ have been fitted by a power law of the kind $N_{A,a} = N^0_{A,a}(1 + t/t_c)^\beta$, where $N^0_{A,a}$ is the doping at $t = 0$ and t_c and β are constants. If the CIGSe layers are treated with RbF-PDT, the relaxed doping $N^0_{A,a}$ is unchanged, but the light-soaking effect becomes stronger. This is more pronounced for the 0.75 GGI sample. The result was confirmed by another set of samples with and without RbF treatment. In consequence, the red-light-soaked state of RbF samples is of higher doping than the one of the untreated samples. The 0.75 GGI sample exhibits a doping concentration above 8×10^{16} cm^{-3}. In Section 6, we will use this effect to study the open-circuit voltage transient upon red light illumination.

4.2 | Higher GGI Increases Bulk Recombination

To reveal the bulk recombination properties of high GGI samples, time-resolved photoluminescence (TRPL) was measured. Figure 4 gives the TRPL transients of untreated and alkali PDT-treated MLU absorbers with different GGIs and different band gaps as derived from the wavelength at 20% EQE (see Section 2). All samples were measured directly after film growth to avoid air-light-induced degradation [56]. Here, we interpret only the rough trend of the decay curves, which could be influenced additionally by a charge separation effect (due to surface band

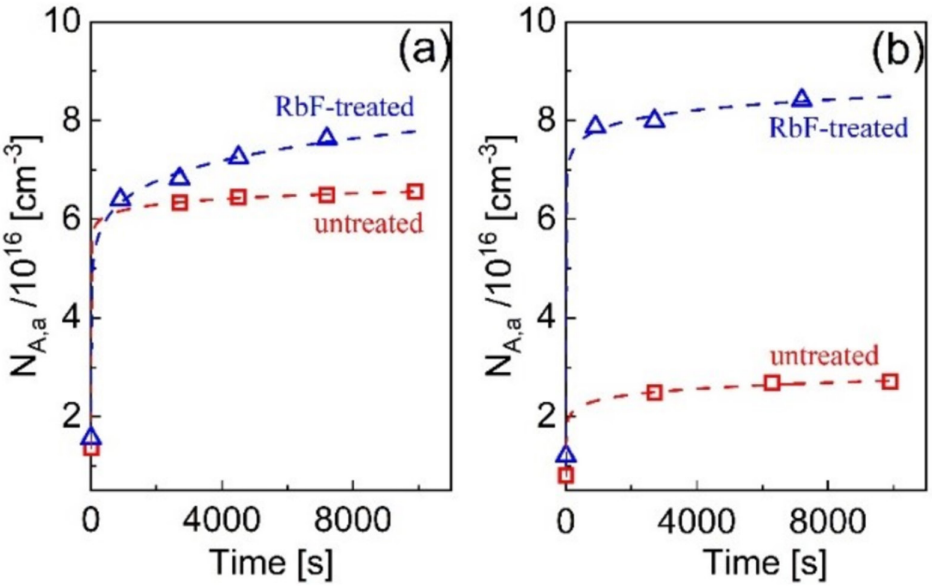

FIGURE 3 | Doping-density transients, as measured by admittance spectroscopy for RbF-treated and untreated (i.e., no PDT) MLU cells with (a) GGI = 0.3 and (b) 0.75. The C(f,t)-measurements were performed in darkness after the respective illumination time by 635 nm light of ½ sun flux equivalent. Dashed lines give a fit to Equation (3) of Ref. [6].

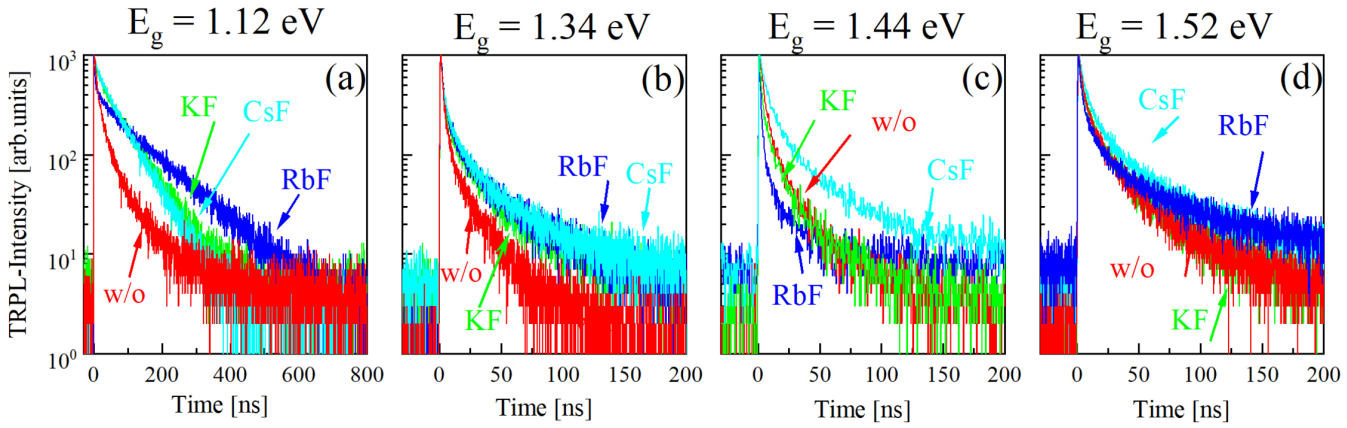

FIGURE 4 | TRPL transients of alkali-treated and untreated MLU absorber layers for different GGI values (a) 0.30 GGI (E_g = 1.12 eV), (b) 0.55 GGI (E_g = 1.34 eV), (c) 0.68 GGI (E_g = 1.44 eV), and (d) 0.78 GGI (E_g = 1.52 eV). Due to the shorter decay times of high versus low GGI absorbers, the time axis of (a) is given on a longer range.

bending) or by a charge carrier trapping effect both prone to give bi-exponential TRPL decay curves [57–59]. (A combination of effects then can even bring curved TRPL transients.) However, we note that both types of effects only can have an influence if the minority carrier lifetime, τ_n, is not too small and exceeds the instrumental function (> 1 ns). In Figure 4, we find that the narrow-gap sample with a GGI of 0.3 (E_g = 1.12 eV) shows the most "linear" (i.e., mono-exponential) decay, also over longer timescales, indicating the longest minority carrier lifetime. For GGI of 0.55 and above, the TRPL transients are much shorter, "curved," and on this low level independent from the exact GGI. The strong (initial) reduction of the minority carrier lifetime values with increasing GGI will also be addressed again in conjunction with Figure 16, where we show a τ_n of 100 ns for the 0.3 GGI sample and a clear reduction of τ_n upon larger GGI, in agreement with the TRPL transients in Figure 4. The calculated τ_n is smaller than 1 ns for GGI ≥ 0.68 ($E_g \geq$ 1.44 eV). Thus, wide-gap CIGSe layers exhibit a higher bulk recombination rate than narrow-gap material.

In Ref. [51], it was pointed out that high-temperature growth improves the performance of wide-gap CIGSe solar cells. In Figure 5, we find a small increase in the TRPL decay time at increased temperature (nominal temperature 675°C instead of 625°C). A further decay time increase can be discerned by the application of an additional NaF precursor on the high-temperature glass. (The role of Na on the TRPL decay of bare absorbers is not completely understood [60].) In summary, the TRPL decay time of high GGI CIGSe layers hardly exceeds the instrumental function (1 ns). It is slightly increased upon high-temperature growth and tailored NaF supply but does not depend on HA treatment. In the MLU laboratory, the TRPL

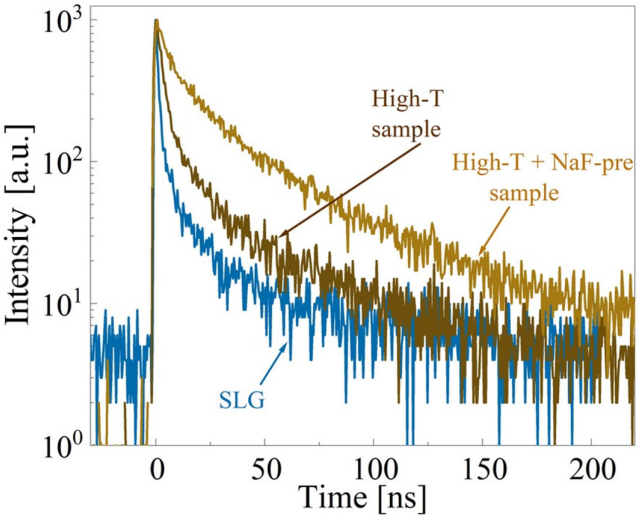

FIGURE 5 | TRPL intensity of alkali-treated MLU CIGSe samples with $E_g = 1.52$ eV, grown on different kinds of glasses. The TRPL signal of the CIGSe absorber grown on Schott glasses with 8 nm NaF-precursor shows the longest minority carrier lifetime.

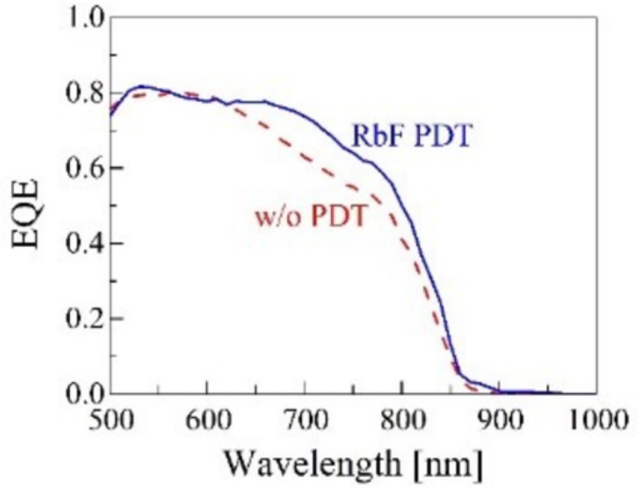

FIGURE 6 | EQE of RbF-PDT treated MLU cell with GGI = 0.8, in comparison with cell without PDT, showing the increase in red EQE.

lifetime measurement at high GGI layers could be used for quality assessment where a longer TRPL decay time is connected with higher device performance.

4.3 | Heavy-Alkali PDT Does Not Reduce Bulk Recombination at High GGI

As mentioned, the 0.30 GGI sample in Figure 4a showed an increase in TRPL decay time upon heavy alkali (HA)-PDT, in accordance with other works [61]. This is true for K, Cs, and Rb, that is, the alkalis being heavier than sodium (justifying the term "HA treatment"). Furthermore, the CsF-treated sample exhibits a PL decay curve that can be fitted by a single exponential with a characteristic time constant of about 70 ns. This lifetime is distinctly larger than that of the CIGSe layer without PDT. In Ref. [24], it was argued that the main effect of alkali PDT on narrow-gap CIGSe devices is related to decreased recombination in the bulk. Now, for GGIs of 0.55 and higher, the TRPL decay curves in Figure 4b–d are hardly influenced by the alkali-PDT. This finding is in agreement with Ref. [1], where samples with large GGI also showed no "alkali effect".

4.4 | Heavy Alkali PDT Increases EQE red Response

HA post-deposition treatment of wide-gap CIGSe leads to increased EQE in the long wavelength range, as already indicated in [62]. The EQEs [62] shown in Figure 6 (different samples than in Ref. [62]) confirm this effect: The short wavelength EQE and the band gaps of both samples are roughly identical. The increased *long* wavelength EQE in Figure 6, together with the increased doping concentration in Figure 3, suggests an increased minority carrier diffusion length of the RbF-PDT MLU CIGSe layers. In combination with the unaltered carrier lifetime, this observation points toward an increased charge carrier mobility perhaps due to altered grain boundary properties.

5 | Interfaces and Grain Boundaries

Using sophisticated surface characterization approaches, it is now well established that the surfaces and interfaces in chalcopyrite devices are particularly complex and require in-depth studies for a correct description. For example, it is not possible to utilize optically derived (tabulated) bulk band gaps to determine (or even estimate) band alignments, since the composition of (high-performance) chalcopyrite absorber surfaces differs from the nominal composition in the bulk, and hence, also, the electronic surface band gap is rather different [7, 12]. Furthermore, when forming the interface to the buffer layer, interface dipoles are formed, in part due to local chemical bonding, but also due to interdiffusion processes between the absorber and buffer layer [63, 64]. Such dipoles are not necessarily taken into account in density functional theory calculations (DFT) [65]· [66, 67] for band alignment estimations. Chalcopyrite absorbers show pronounced band bending toward their surfaces, which can sometimes, but not always, be further enhanced by the interface formation with the buffer. While common at semiconductor surfaces, such a band bending should not be misinterpreted as a modification of fundamental materials properties, such as the "position" of band edges with respect to an energy reference level when external parameters (here: the GGI) are modified. Rather, it is a complex interplay between a variety of surface effects, requiring a detailed analysis of the particular surface under study. To thus *directly* determine the chemical and electronic structure at the surface of ZSW absorbers with different GGI ratios and their interfaces with CdS, we have used XPS, UPS, and IPES on a number of absorber and interface samples with varying GGIs (note that the here-studied surfaces have not been subjected to a PDT).

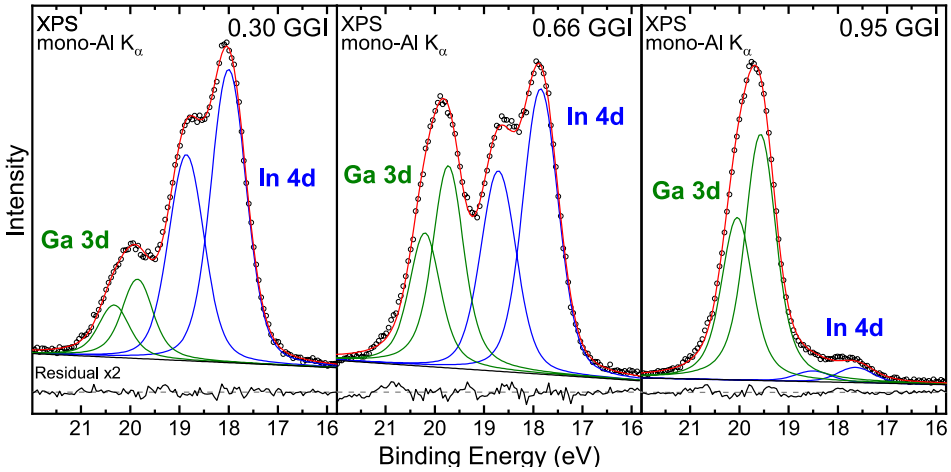

FIGURE 7 | Monochromatized Al K_α spectra of the In4d/Ga 3d region of 0.30, 0.66, and 0.95 GGI CIGSe absorbers (without PDT). The Ga 3d and In 4d components are shown in green and blue, respectively. The magnified (×2) residuals are shown below each spectrum.

TABLE 1 | Comparison of bulk and surface GGI and [Cu]/([Ga] + [In]) (CGI) ratios, as well as bulk and surface band gaps as a function of GGI. CIGSe samples were not treated with a PDT.

Bulk GGI from XRF:	**0.30 ± 0.01**	**0.66 ± 0.01**	**0.95 ± 0.01**
Surface GGI (from XPS):	0.36 ± 0.06	0.63 ± 0.07	0.97 ± 0.01
Bulk E_g (from EQE)	1.16 (± 0.02) eV	1.37 (± 0.02) eV	1.62 (± 0.02) eV
Surface E_g (from UPS/IPES)	1.45 (± 0.18) eV	—	1.96 (± 0.18) eV
Surface E_F-E_{VBM} (from UPS)	0.75 (± 0.10) eV	0.71 (± 0.10) eV	0.58 (± 0.10) eV
Bulk CGI (from XRF):	0.85 ± 0.01	0.88 ± 0.01	0.95 ± 0.01
Surface CGI (from XPS):	0.51 ± 0.09	0.49 ± 0.09	0.68 ± 0.09

5.1 | Band Gap Widening at the CIGSe Surface Also for High GGI

Figure 7 displays the Ga 3d/In 4d XPS spectra (excited by monochromatized Al K_α) for three different GGI ratios (0.30, 0.66, and 0.95). With increasing nominal (bulk) GGI, we find the In 4d and Ga 3d intensities to decrease and increase, respectively. To quantify this, the three datasets were simultaneously fitted using a linear background and Voigt profiles. Both doublets (In $4d_{3/2}/4d_{5/2}$ and Ga $3d_{3/2}/3d_{5/2}$) were described by two Voigt profiles with equal Lorentzian and Gaussian contributions and a fixed intensity ratio of 2:3 according to the 2j + 1 multiplicity. The spin-orbit splitting was used as a fitting parameter but kept equal throughout this GGI series. To calculate the surface GGI, we considered the corresponding photoionization cross-sections [68], while the inelastic mean free path λ and analyzer transmission function, being a function of the electron kinetic energy and thus approximately equal for In 4d and Ga 3d, did not have to be taken into account. In Table 1, the derived surface GGIs are compared with the bulk values (as determined by X-ray fluorescence, XRF)—they are identical for each sample (within the error bar). Therefore, surface analysis does not reveal a Ga or In enrichment at the very surface. The results can be compared with the GDOES depth profiles in Figure 1c where the front surface GGI also roughly agreed with the respective bulk value.

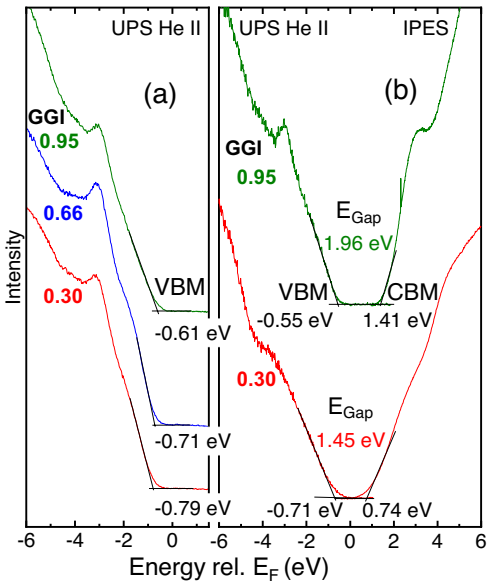

FIGURE 8 | (a) UV photoelectron spectroscopy (UPS) of CIGSe samples with GGI = 0.30 (red), 0.66 (blue), and 0.95 (green), measured at KIT; (b) UPS and inverse photoemission spectroscopy (IPES) data for GGI = 0.30 (red, bottom) and 0.95 (green, top), measured at UNLV. Valence and conduction band extrema are determined with a linear extrapolation of the leading edge. No PDT was applied to these samples.

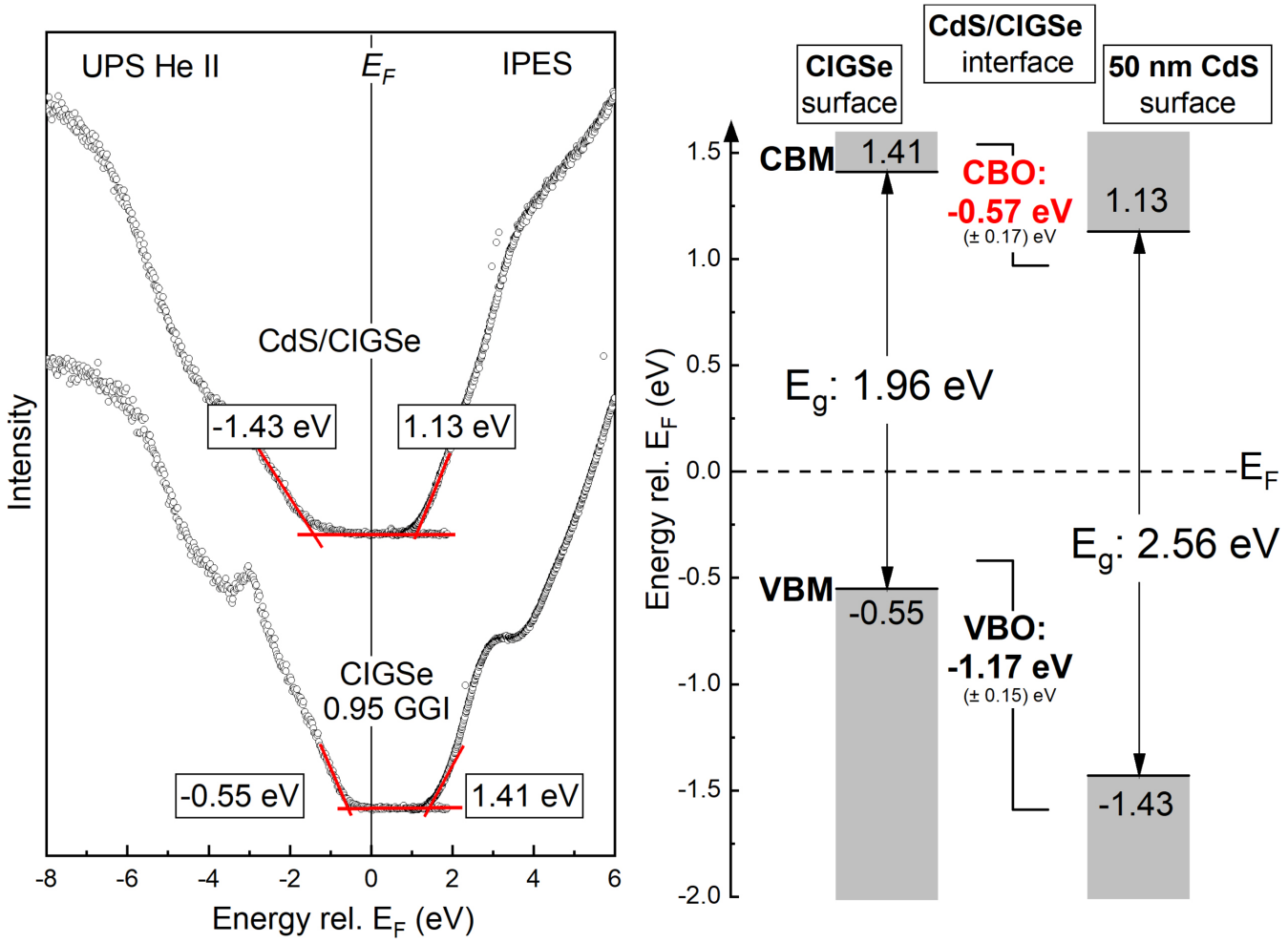

FIGURE 9 | Left: UPS/IPES spectra of the GGI = 0.95 CIGSe absorber and the corresponding CdS/CIGSe sample. Linear extrapolations are drawn to determine the valence and conduction band edges. Right: Schematic band diagram of the CdS/CIGSe interface for GGI = 0.95.

To gain further insights into the local chemical environments at the surface, the modified indium Auger parameter α'_{In} was determined by adding the In $3d_{5/2}$ binding energy and the kinetic energy of the In $N_4M_{4,5}M_{4,5}$ Auger feature. The value of $\alpha'_{In} = 852.57 \pm 0.05$ eV for the 0.3 GGI sample is in good agreement with tabulated and our own values for Cu (In,Ga)$(S,Se)_2$ absorber surfaces ($852.40 \leq \alpha'_{In,CIGSSe} \leq 852.70$ eV) [11, 69–71]. For increasing GGI, the value of α'_{In} decreases, to $\alpha'_{In} = 852.48 \pm 0.10$ eV for the 0.66 GGI sample and $\alpha'_{In} = 852.20 \pm 0.15$ eV for a GGI of 0.95. This suggests that the increasing Ga concentration also affects the local chemical environment of In (either through direct In-Ga bonds or through next-neighbor interactions).

To study the impact of the GGI on the electronic structure, UPS and IPES measurements were performed on the different GGI absorber surfaces. Figure 8a shows the UPS valence band region of samples with GGI = 0.30, 0.66, and 0.95, while Figure 8b shows UPS/IPES spectra of the GGI = 0.30 and 0.95 absorbers (only). We note that the absorber surfaces were measured in different experimental setups (Figure 9a: KIT; Figure 9b: UNLV) and, correspondingly, after slightly different "histories" of the sample surfaces, which leads to small variations in the valence band maximum, VBM. The VBM and conduction band minima (CBM) were determined with linear extrapolations of the leading edge of each spectrum [72, 73]. In Table 1, the values are summarized and compared with bulk E_g values (note that for the GGI = 0.3 and 0.95 samples, the VBM values are averaged over the two different experiments). For increasing GGI, the VBM at the surface shifts toward the Fermi energy. For the 0.3 GGI absorber, the Fermi energy E_F is approximately in the middle of the band gap at the sample surface. In contrast, the VBM of the 0.95 GGI sample surface is closer to E_F and shows a larger band gap than the 0.30 GGI absorber at its surface. In addition, the absorber surface band gaps of the 0.30 and 0.95 GGI absorber surfaces are roughly ~0.30 eV larger than the EQE-determined bulk band gaps (see Table 1), which can likely be related to a Cu-deficient surface stoichiometry. The corresponding surface CGI ratio (determined using Cu 3p, Ga 3d, and In 4d) is considerably smaller than the bulk values, showing a surface Cu depletion *independent* of the GGI [49, 74]. In Ref. [75], it was shown that for $CuGaSe_2$ surfaces, an upward shift of E_F can lead to Cu depletion. This was supported by solid state theory in Refs. [19, 76], where the spontaneous formation of p-type doping copper vacancies was predicted for a Fermi energy exceeding 0.8 eV above VBM. Here, the surface E_F^{if}–E_{VBM}^{if} of the 0.95 GGI absorber (0.58 eV, see Table 1) is smaller than the value 0.8 eV for spontaneous V_{Cu} formation.

5.2 | A Conduction Band "Cliff" at the CdS/Wide-Gap CIGSe Interface

The band alignment at the interface between CdS and the 0.95 GGI CIGSe sample was derived by complementing the UPS/IPES measurements of the GGI = 0.95 absorber in Figure 8b by those of the full CdS buffer layer on top of the absorber (CdS/CIGSe), shown in Figure 9 (left). We find a band gap of 2.56 (±0.18) eV at the surface of the 50-nm CdS/CIGSe sample, with E_F slightly above mid-gap. To derive the band alignment, the additional band bending induced by the interface formation needs to be taken into account. For this purpose, we used a thin buffer layer sample, for which the absorber-related photoemission peaks can still be detected with XPS. The relative shifts of the absorber-related peaks (e.g., Ga 2p, In 3d, Se 3d) and buffer-related peaks (e.g., Cd 3d and S 2p) are analyzed and used to deduce the VBM and CBM values at the interface from the values at the CIGSe and CdS surfaces. As summarized in Figure 9 (right), we find a significant negative conduction band offset of −0.57 (±0.17) eV (i.e., a cliff) and a valence band offset of −1.17 (±0.15) eV. This electronic structure could foster interface recombination in the device in case of sufficiently high interface defect density. For a more quantitative discussion (see below), we now label the difference between the CdS CBM and the CIGSe VBM as "interface 'band gap'." While not a band gap in the true electronic (*k*-dependent) sense, since the two band edge states are not fully delocalized at the same point in real space, this number lends itself to a comparison with the involved band gaps and, potentially, the observed open-circuit voltage and extrapolated low-temperature activation energies. Here, the interface "band gap" amounts to 1.39 eV, which is smaller than the optically derived absorber bulk band gap of 1.62 eV and—by the amount of the CBO—considerably smaller than the electronic CIGSe surface band gap of 1.96 eV (as expected).

The CIGSe surfaces examined up to this part of the paper were not treated by a PDT step. Elsewhere, we report that the conduction band alignment of a CdS/RbF-PDT CIGSe interface with an absorber GGI of 0.90 shows a CBO of −0.53 eV [4]. This observation indicates that the RbF-PDT, as employed by ZSW, does not impact the conduction band alignment for high GGI absorbers, as was previously found for low-GGI ZSW absorbers as well [10, 25].

5.3 | Heavy Alkali (HA) PDT Could Lead to HA-In-Se Bonds at the Absorber Surface

It has been found earlier for narrow-gap CIGSe films that a heavy alkali treatment can, among other effects, increase the open-circuit voltage (V_{oc}) [77]. In some cases, however, this gain is compensated by a fill factor loss [78]. The reason for the loss is a distortion of the JV curve, which was attributed to a charge transport barrier. This barrier may, among others, be due to (1) HA-In-Se-type bonds at the absorber surface [79] or (2) a barrier at the back contact [80]. Indications for a HA-In-Se type surface were found for KF-PDT on EMPA absorbers by Handick et al. [81]. A surface band gap of 2.52 eV was proposed, which would be in close agreement with the $KInSe_2$ bulk band gap of 2.7 eV [82]. A distinct $HAInSe_2$ phase could, so far, only be detected at the buffer/CIGSe interface in one TEM study [26], and no evidence for a similar effect for pure $CuGaSe_2$ absorbers has been found, even if the existence of a $KGaSe_2$ phase (in general) has been reported [83]. Also, an HA effect on the solar cell performance could not be found for $CuGaSe_2$ [1]. Therefore, one idea of incorporating indium in wide-gap CIGSe is to allow the formation of HA-In-Se bonds at the absorber surface phase, which may mitigate interface recombination. Of course, a possible HA-In-Se environment at the surface of a high GGI absorber should not lead to barrier behavior.

Figure 10 shows typical results of STEM analyses of the front interface region of an MLU CIGSe device with a GGI of 0.80 and a CGI of 0.90, with CBD-CdS buffer on top. An apparent increase in the Rb and In signals (Rb maximum is marked by a vertical dashed line), together with a right shift of the Se signal drop, can be seen in Figure 10b. The Ga and Cu signals drop further left of the dashed line. Thus, enrichment of Rb, In, and Se at the CdS/CIGSe interface is detected, which could be confirmed by APT proximity histograms [84]. If Rb

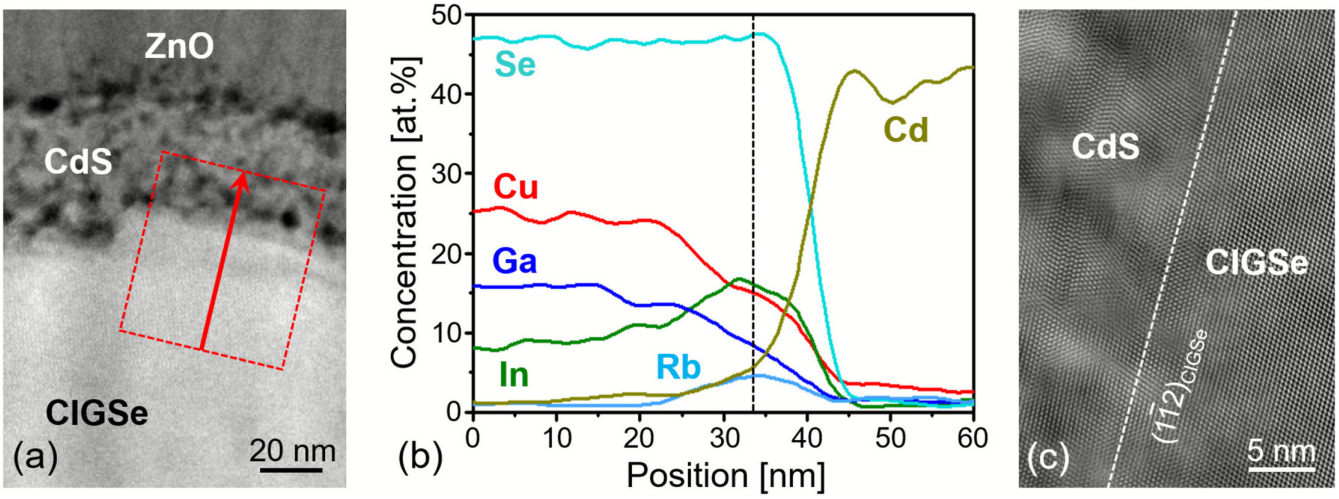

FIGURE 10 | (a) STEM HAADF image of the CIGSe/CdS/ZnO layer stack, as prepared by MLU. The CIGSe absorber has a GGI of 0.80 and was treated by 25 nm RbF, as described in the experimental section. The dotted rectangle marks the area of integrated EDXS line scans along the red arrow. (b) Quantification of integrated line scans along red arrow in (a). A vertical dashed line gives the position of maximum Rb concentration. (c) High-resolution STEM HAADF image of the CdS/CIGSe interface along the <110> zone axis of CIGSe.

were to be dissolved in CIGSe at the interface (and would not form a distinct compound), the depletion from Cu and Ga would be difficult to explain. However, inspection of the interface by high-resolution STEM HAADF[2] at several locations (see example in Figure 10c) did not reveal the typical layered structure of $RbInSe_2$ that has been found in Ref. [26]. We conclude that a distinct $RbInSe_2$ phase with space group C2/c [85] is either absent, too thin, or too discontinuous to be detected. In Refs. [86, 87], no Raman modes were detected for HA-PDT surfaces, which were attributed to the formation of an amorphous $HAInSe_2$ phase [88]. However, in Figure 10c, amorphous structures at the CdS/CIGSe interface are also missing. Therefore, in the following, we speak of a Rb-In-Se-containing environment (rather than a separate layer, phase, or compound) at the surface of RbF-treated MLU absorbers.

5.4 | Indium-Enriched Wide-Gap Grain Boundaries

While indium enrichment was a phenomenon at the buffer/wide-gap CIGSe interface of the MLU sample investigated above, one may ask if a similar trend applies for grain boundaries. This is indeed visible in the typical APT 3D maps and the corresponding proximity histograms of related MLU samples shown in Figure 11, where (a) represents a Cu-poor and (b) a Cu-rich grain boundary. It can be seen that in (a), the Cu depletion is combined with a slight Se enrichment, very little Ga enrichment, but a relatively strong In enrichment. These trends are very similar to the ones observed for the Cu-poor grain boundaries in low GGI CIGSe films [40, 89]. Nevertheless, the grain boundary preserves a relatively high GGI value. For the Cu-rich grain boundary in Figure 11b, Ga depletion balances the Cu enrichment, but surprisingly, In depletion is not observed. Therefore, indium atoms appear to decorate several forms of grain boundaries in high GGI CIGSe absorbers.

Recently, it has been proposed that Cu-rich grain boundaries with a positive Cu-factor $\Delta\beta$ ($\Delta\beta = \Delta Cu - (\Delta Se + \Delta In + \Delta Ga)$ where $\Delta X[\%] = [X \text{ at GB}] - [X \text{ in grain interior}]$ and X = Cu, In, Ga, or Se) are electrically detrimental, exhibiting a reduction in electron beam induced current collection, whereas those with negative $\Delta\beta$, that is., with Cu-poor grain boundaries, show an opposite behavior [89]. Interestingly, the fraction of Cu-rich grain boundaries in high GGI CIGSe absorbers is notably higher (27%) than in low GGI CIGSe absorbers (16%) [40], suggesting that the grain boundaries in high GGI absorbers have to be further optimized to obtain solar cells with better performance. A further observation addresses the concept of sodium accumulation at

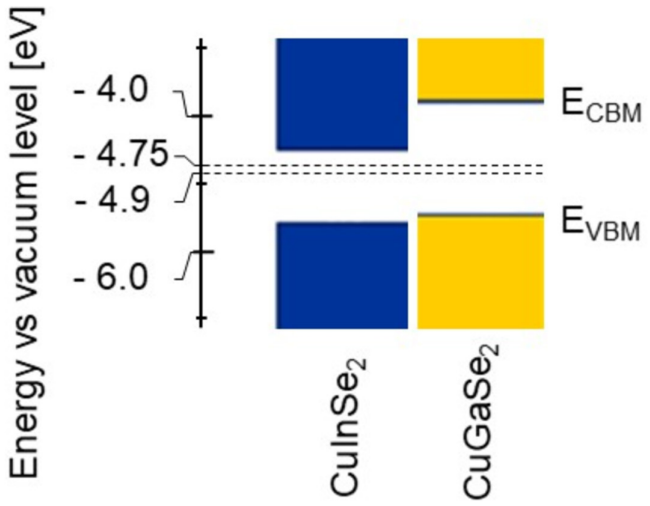

FIGURE 12 | DFT-derived band edges of $CuInSe_2$ and $CuGaSe_2$ from Ref. [66] (calculated with respect to an assumed vacuum level) and local KPFM-derived work functions of 4.9 and 4.75 eV for untreated and RbF-treated samples, respectively, from Ref. [36] and Figure S3.

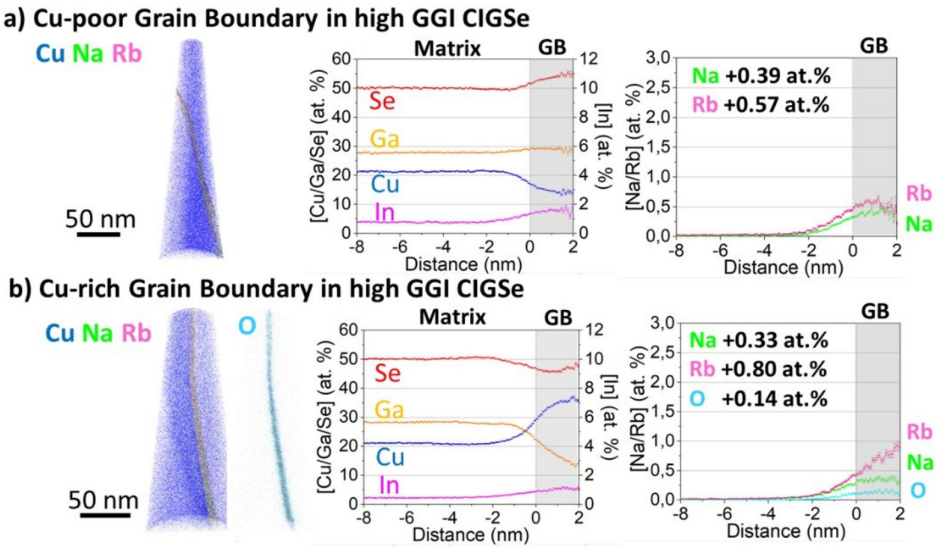

FIGURE 11 | APT 3D maps and the corresponding proximity histograms of two representative grain boundaries (GBs): (a) Cu-poor and (b) Cu-rich grain boundaries (GBs) in a wide-gap (GGI = 0.9) MLU CIGSe absorber treated by RbF-PDT. Note the indium compositions are given on the right axis of the proxigrams labelled "Matrix Elements." The dopant compositions are given separately in the proxigrams labelled "Dopants." All proxigrams were built using a Cu iso-surface with an iso-composition value of 27 and 29 at.%, respectively.

grain boundaries. Here, this effect appears to be much smaller in high GGI CIGSe absorbers (~0.3 at.%) than in the low GGI CIGS absorbers (~0.6 to 1 at.%). Oxygen enrichment appears to be always correlated with Cu-rich grain boundaries, in agreement with previous studies [38, 40, 89].

5.5 | HA PDT Leads to Larger Hole Barrier at Grain Boundaries

In Ref. [90, 91], it was shown that in narrow-gap CIGSe, HA elements can be enriched at grain boundaries. In Figure 11, we found the same trend for wide-gap CIGSe layers of MLU with a clear increase in the Rb signal at grain boundaries. So far, no clear evidence for HA-induced electronic passivation of grain boundaries could be obtained [92]. In Ref. [93], an electron barrier was determined by KPFM, which could reduce grain boundary recombination. Here, we engross the KPFM cross-section experiments previously reported in Ref. [36]. Figure S3 replots the KPFM data from cross-sections of different MLU CIGSe thin films. An exemplary surface potential difference map for a sample with GGI = 0.3 and PDT is shown in Figure 2b of Ref. [36]. There are two findings from Ref. [36]: (1) The untreated layers with GGI = 0.8 and 0.3 both exhibit Φ_{CIGSe} of around 4.9 eV. In Figure 12b, we have plotted the work functions Φ_{CIGSe} on the energy scale relative to the

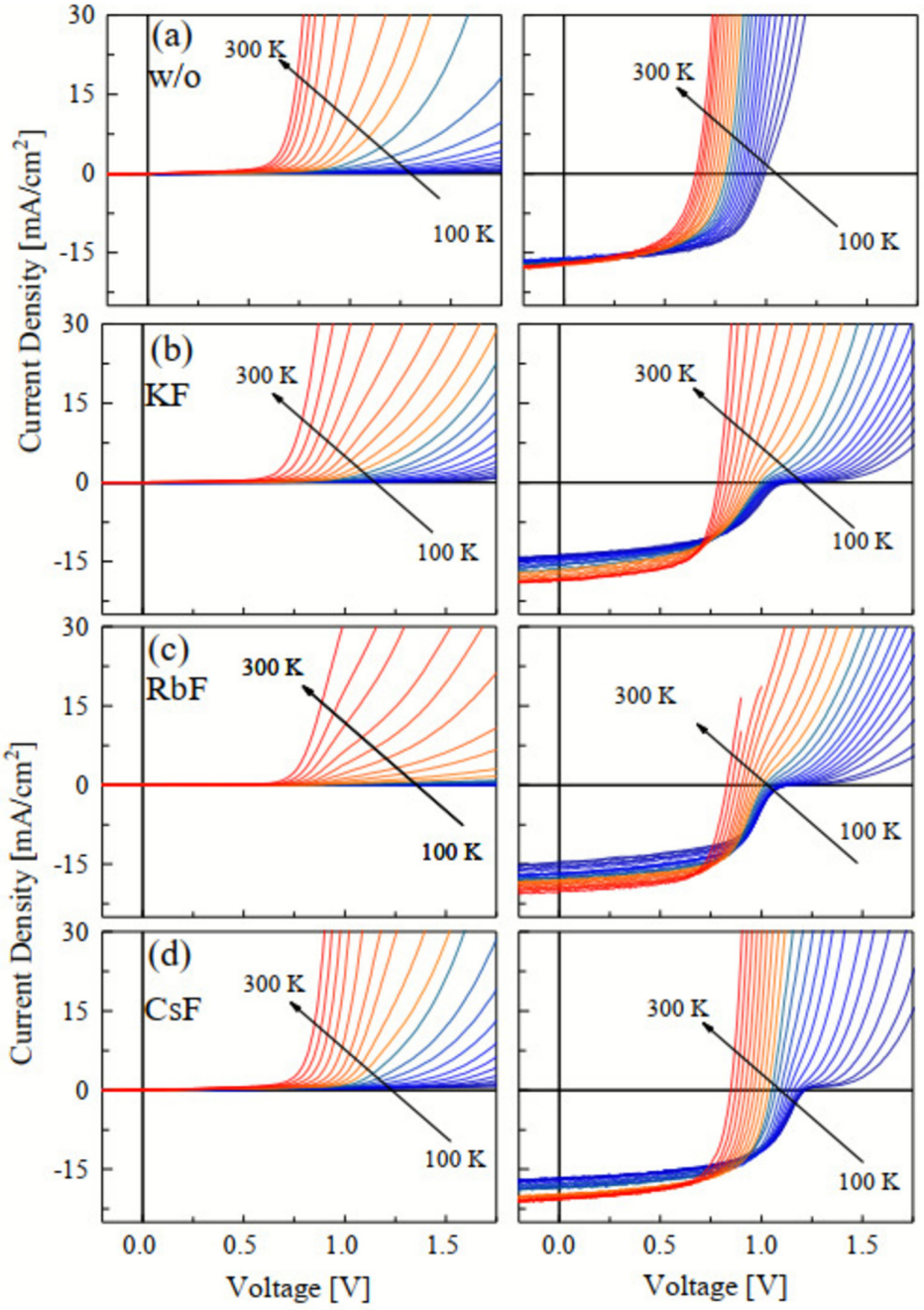

FIGURE 13 | Dark (left) and white light illuminated (right) JV curves at different temperatures for MLU CIGSe solar cells from (a) untreated, (b) KF-treated, (c) RbF-treated, and (d) CsF-treated absorbers with GGI = 0.87 ± 0.02 and optically-derived band gap E_g = 1.44 eV.

band edges of $CuInSe_2$ and $CuGaSe_2$ as calculated by DFT in Ref. [66]. Assuming a p-doped bulk, one can deduce a downward band bending toward the CIGSe grain boundary. This band bending would represent a hole barrier and not an electron barrier. Due to a higher VBM, the band bending may be smaller for the large GGI sample in absolute terms. Due to the larger band gap of the large GGI sample, it is much smaller in relative terms compared with the low GGI band bending. (2) Upon RbF treatment, a slight reduction in the work function to $\Phi_{CIGSe} \approx 4.75$ eV was found in Ref. [36] and Figure S3. This would indicate that the RbF treatment slightly increases the hole barrier at grain boundaries both for low and high GGI films of CIGSe. (Our findings, however, are in contrast to the dominant electron barrier found by surface KPFM scans for RbF PDT treated CIGSe in Ref. [93].) A hole barrier promotes carrier recombination at grain boundaries of p-type semiconductors. Increasing this barrier height would further increase the recombination of minority carriers at grain boundaries, unless the recombination rate is limited by defect saturation. In the TRPL study presented in Figure 4, we observed no clear change in bulk recombination upon HA-PDT for wide-gap CIGSe. Because the increase in the hole barrier upon HA-PDT is small, the KPFM result does not exclude grain boundary dominated recombination in wide-gap CIGSe.

6 | Devices

Standard heterojunction solar cells have been prepared with the stacking sequence Mo/CIGSe/CdS/ZnO/TCO, where TCO was either ZnO:Al or ITO. It is instructive to investigate the performance of devices with CdS buffer layers prepared by chemical bath deposition by means of $V_{oc}(t)$ transients to test if wide-gap CIGSe devices without and with HA PDT are limited by interface recombination. At the end, the properties of laboratory cells are compared with those from an industrial process.

6.1 | HA PDT Supports the Formation of a Current Barrier

Figure 13 shows the dark and light JV curves for untreated (without) as well as HA fluoride-treated MLU devices (HA = K, Rb, and Cs) with a global GGI of 0.87 ± 0.02 and an optically derived band gap E_g of 1.44 eV. Similar to Ref. [45] for the KF-treated devices, we find for RbF and CsF (i) a double diode behavior, or partial current blocking under forward bias, and (ii) a temperature-dependent photocurrent. In addition, (iii) a V_{oc} saturation for the HA PDT-treated devices can be discerned, while this saturation is absent for untreated cells. The $V_{oc}(T)$ data were extracted and plotted in Figure 15a. This figure corroborates the onset of $V_{oc}(T)$ saturation for low temperatures in the case of HA treatment, but not in the case of untreated devices. (The results in Figure 15 could be reproduced by a second set of MLU samples.) Hence, all HA elements lead to the identical phenomena (i), (ii), and (iii). On the other hand, all devices, including the one without PDT, exhibit (iv) a crossover of dark and illuminated JV curves. The crossover phenomenon is common for CIGSe solar cells and may be due to a bias-dependent potential barrier, which can be explained by either deep acceptor states in CdS with highly asymmetric capture cross-sections [94] or by a p^+ layer at the CIGSe surface [95]. Phenomena (i) and (iii), however, may share a different origin than the crossover phenomenon (iv).

As pointed out in Ref. [45], the double diode behavior for KF-treated devices could be simulated by a postulated $KInSe_2$ surface layer of 10 nm thickness having a band gap above 2 eV. This concept is similar to the interpretation of Weiss et al. for narrow-gap CIGSe [79]. As we only identified a distinct HA-In enrichment but no distinct HA-In-Se phase in the present work, we continue to speak of a HA-In-Se environment between CIGSe and CdS. Assuming that such a HA-In-Se environment exhibits a lowered valence band maximum, it is able to explain also the resumption of the current at higher voltage bias (double diode behavior, see figure 9 in [45]) as well as the V_{oc} saturation [45]. Below, we show that a HA–In–Se environment with a hypothetical low valence band maximum may in addition explain the modification of the $V_{oc}(t)$ transients upon HA-PDT. On the other hand, the partial blocking of the forward current and the $V_{oc}(T)$ saturation could also be due to a potential barrier at the back contact that becomes larger upon HA-PDT. Several studies have emphasized the role of a back contact barrier in CIGSe solar cells [96–98], mostly for low GGI samples. Such barrier shows up as a capacitance step in admittance spectra [98]. Indeed, in reference [99], wide-gap MLU devices showed a respective capacitance step, which in this reference is labelled as N_1. The step is temperature activated of Arrhenius type. In Ref. [99], the activation energy becomes smaller under rubidium doping also for the wide-gap CIGSe samples. This would indicate a reduced back contact barrier upon RbF treatment—in contrast to the finding in Figure 15. This would favor a HA-In-Se interlayer as in Ref. [45] for the explanation of phenomena (i) and (iii).

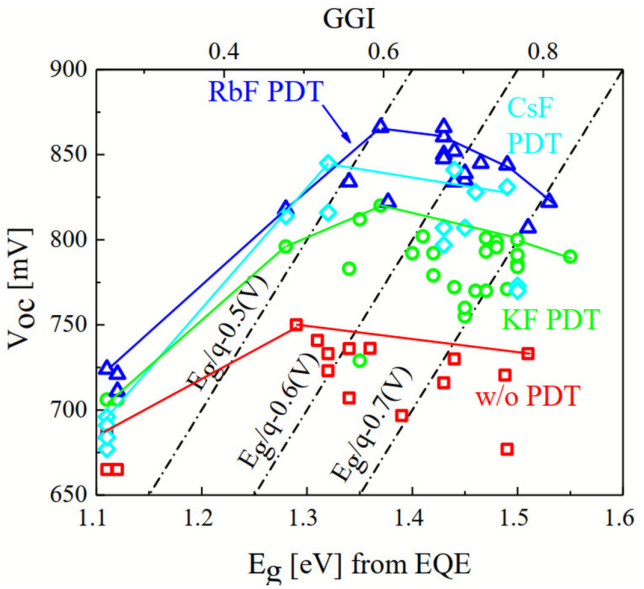

FIGURE 14 | Open circuit voltage V_{oc} of HA PDT and untreated MLU CIGSe solar cells with different GGI and band gap (from EQE). Dashed lines mark iso-loss of 0.5, 0.6, and 0.7 V with respect to the band gap equivalent E_g/q.

Regarding Figure 13, phenomenon (ii) (i.e., the temperature-dependent photocurrent) remains to be discussed. Being also generic for all HA post-deposition treatments, we follow the interpretation of Pianezzi et al. [100], who assume a shallow donor state below the conduction band of CIGSe that is introduced by the HA PDT and which, depending on the temperature, acts as a trap (high T, large J_{sc}) or a recombination center (low T, small J_{sc}). The effect was already simulated for KF treatment in Ref. [45].

6.2 | Substantial V_{oc} Increase for HA PDT of Wide-Gap CIGSe

Figure 14 shows the GGI influence on the open-circuit voltage V_{oc} for cells with different HA PDTs, in comparison with untreated CIGSe cells. The absorbers were grown with the modified three-stage process by MLU, as explained in Section 3. While there is little increase in V_{oc} for the narrow-gap HA PDT

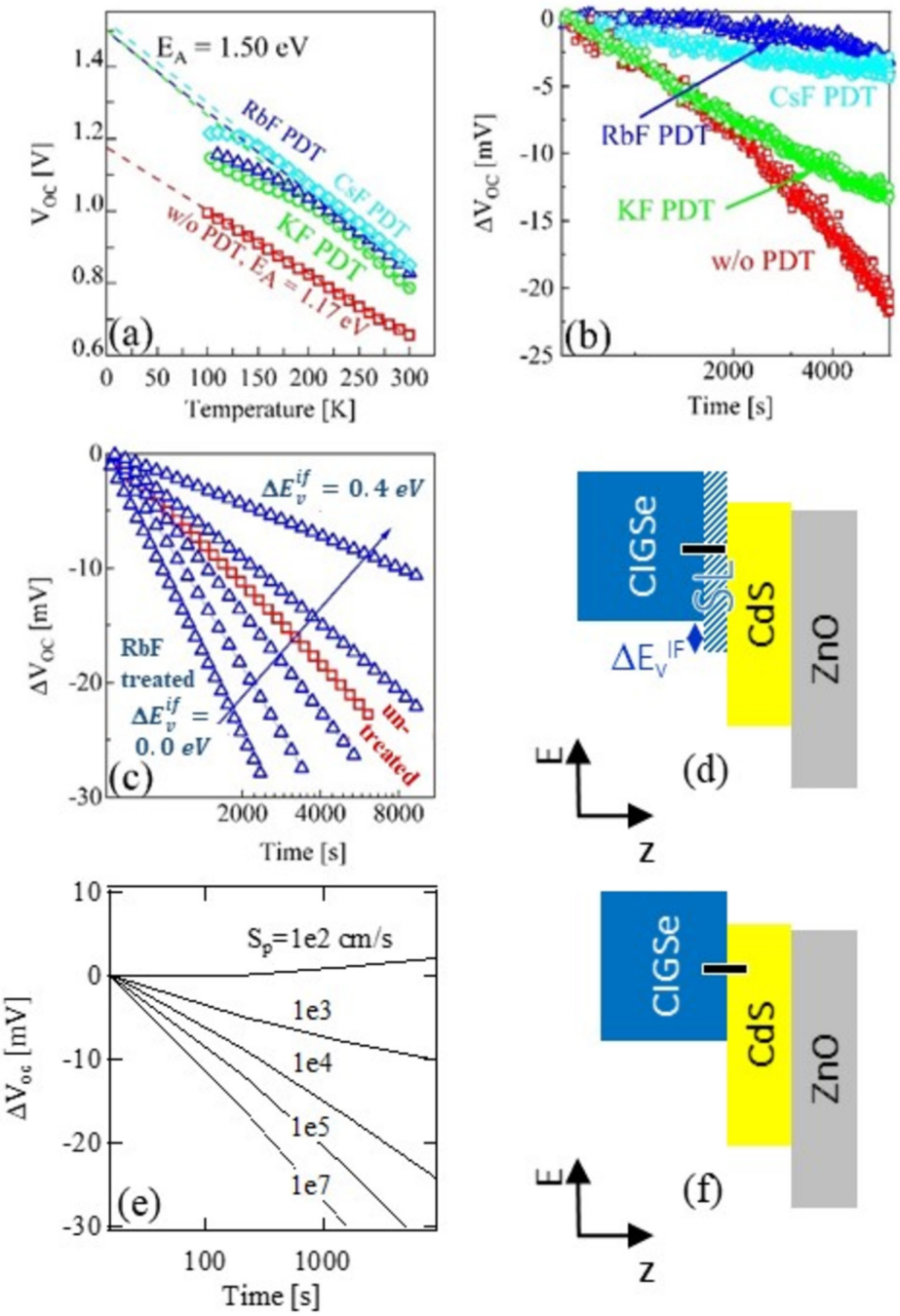

FIGURE 15 | (a) Experimental temperature-dependent $V_{oc}(T)$ for wide-gap CIGSe/CdS/i-ZnO/ZnO:Al MLU cells with GGI = 0.87 ± 0.02 and E_g = 1.44 eV. Dashed lines give linear fits of the high-temperature range. (b) Experimental time-dependent $\Delta V_{oc}(t) = V_{oc}(t) - V_{oc}(t_0)$ with t_0 = 630 s for the same devices as in (a) under constant red light illumination (xenon lamp solar modulator AM1.5, 1000 W/m^2 with an optical cut-off filter $\lambda > 630$ nm) at room temperature. (c) Simulated $\Delta V_{oc}(t)$ transients using the experimental time series of $N_{A,a}(t)$ from Figure 3 with different valence band offsets in an assumed device structure CIGSe/SL/CdS/ZnO, as depicted in (d), where SL denotes a surface layer with band gap of $E_{g,CIGSe} + \Delta E_v^{if}$. (e) Simulated $\Delta V_{oc}(t)$ transients with different recombination velocities at an assumed interface defect as depicted in (f).

samples in comparison to the untreated devices, the increase is strongest for a GGI around 0.6, that is, a band gap around 1.4 eV. There, RbF and CsF appear to be most efficient for achieving a higher V_{oc}. Below, we show that RbF will also lead to very efficient wide-gap devices.

In Ref. [62], it was shown that all HA PDT cells exhibit an increased long wavelength response of the EQE. Together with the larger absorber doping shown in Figure 3, which would rather shrink the SCR and thus the collection length, this points to a larger diffusion length upon HA doping. Despite the remarkable V_{oc} effect due to the HA PDT, it is apparent from Figure 14 that the V_{oc} deficit (in the figure exemplified by reference to the band gap) becomes larger for all curves with increasing GGI.

6.3 | HA PDT Has an Impact on Interface Recombination

In the case of narrow-gap CIGSe, the positive HA effect on the cell performance was explained by bulk modifications, such as increased doping and higher carrier lifetime [24]. This is in agreement with the general finding that high-efficiency narrow-gap CIGSe solar cells are likely not limited by interface recombination—in contrast to wide-gap CIGSe cells with a CdS buffer layer [6]. For wide-gap CIGSe, there is the question of whether HA PDT affects the interface recombination. In order to identify the dominance of interface recombination, the activation energy E_A of the saturation current derived from extrapolated $V_{oc}(T)$ is investigated. In Figure 15a, the device without PDT exhibits $E_A < E_g$, where E_g is the absorber bulk band gap. This suggests that recombination at the CIGSe/CdS interface dominates (see section 7.3.2 in Ref. [49]), in agreement with many earlier findings [6, 51, 99]. As an exception, in the literature, there is the report of $E_A = E_g$ [101]. The latter may be a result of very high bulk recombination even exceeding interface recombination. In our case, the extrapolated value of $V_{oc}(0\,K) = 1.17$ eV is significantly lower than all band gaps (bulk or interface) discussed above. All HA-treated MLU devices to the contrary exhibit extrapolated open-circuit voltages of $V_{oc}(T \rightarrow 0) = E_g$. At this point, we note that, according to Ref. [102], interface recombination is not excluded for $E_A = E_g$. To differentiate interface recombination from bulk recombination, open-circuit voltage transients $V_{oc}(t)$ can be employed for CIGSe solar cells, making use of the inherent doping metastability of the CIGSe layers [6]. The existence of doping metastability in wide-gap CIGSe was already concluded from Figure 3: The wide-gap CIGSe doping increases with illumination time. A resulting negative $V_{oc}(t)$ transient upon increasing illumination time can be due to interface recombination or tunneling-enhanced recombination in the space-charge region [103]. Figure 15b shows that all devices with GGI = 0.8 have a negative slope; that is, V_{oc} decreases with increasing illumination time. Tunneling-enhanced recombination [103] in the space-charge region can be excluded for these devices due to too low doping (see Figure 3) and due to their diode quality factor A being smaller than 2. Thus, one can suggest that the dominant recombination for all devices takes place at the interface, albeit with different activation energies.

In Ref. [20], it was shown on a large set of KF-treated MLU samples that some KF-treated cells may well exhibit positive $V_{oc}(t)$ slopes. In addition, $E_A = E_g$ was repeatedly observed where E_g is the band gap of the CIGSe layer. This suggests that the CIGSe/CdS interface can be passivated by a HA PDT up to the complete suppression of interface recombination. However, complete suppression of interface recombination is not observed for the sample set in Figure 15b, since all slopes of $V_{oc}(t)$ are negative. On the other hand, we find in Figure 15b that the $V_{oc}(t)$ slope becomes smaller upon HA treatment. This is concomitant with a higher V_{oc} in Figure 13 of the HA-treated devices. In Figure 15c,e, two models were tested for their possible explanation of the varied $V_{oc}(t)$ slopes: a model employing a surface layer (SL), which lowers the valence band at the CIGSe surface (see sketch in d) and a model with modified defect density, or recombination velocity, at the CIGSe/CdS interface (sketch in f). Here, the measured time development of the absorber doping from Figure 3 was taken as input for the computer simulation (see Section 2). Both models can explain the higher V_{oc} (enabled by reduced interface recombination) and the reduced negative slope of $dV_{oc}(t)/dt$. Both models essentially reduce the hole recombination rate at the interface being the limiting step at this presumed inverted interface (electrons are majority carriers and holes are minority carriers). The hole recombination rate depends on the interface hole density p times the hole recombination velocity S_p. Model (d) uses a decreasing hole concentration p at the interface by decreasing the valence band edge. Model (f) just reduces the recombination velocity S_p, which can result from either a reduced defect density or a reduced hole capture cross-section [4]. In the case of the surface layer model (d) in Figure 15, phenomena (i), which is the partial current blocking, and (iii), which is the $V_{oc}(T)$ saturation, would be simultaneously explained [45].

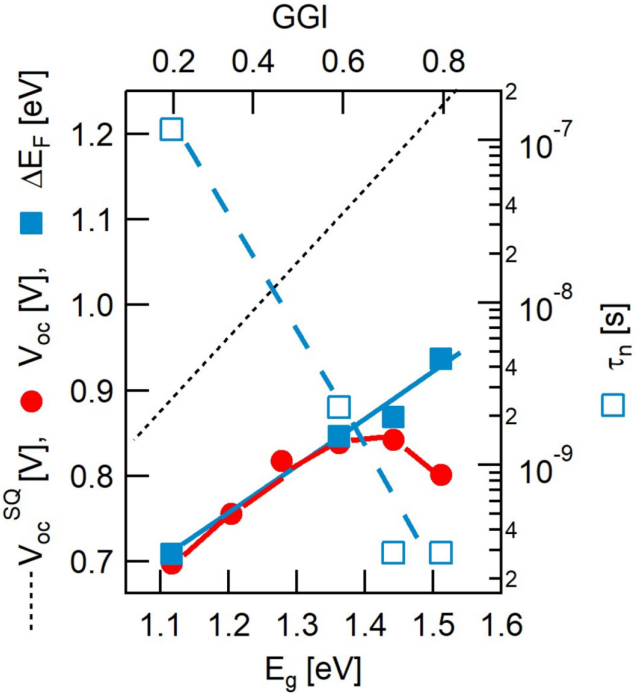

FIGURE 16 | Open-circuit voltage V_{oc} and quasi Fermi-level splitting ΔE_F of MLU devices, in comparison with the theoretical limit V_{oc}^{SQ}. Electron lifetime τ_n derived from ΔE_F of Rb-treated MLU CIGSe layers and solar cells using the PLQY method.

6.4 | Open Circuit Voltage Deficit Increases With Band Gap

In order to assess the V_{oc} deficit for MLU devices with different GGI, steady-state, absolute quantified photoluminescence experiments (PLQY) were conducted and the quasi-Fermi level splitting was inferred from fitting the high-energy slope of the photoluminescence spectra [104]. The experiments were performed on bare CIGSe layers but in N_2 in order to avoid degradation. Figure 16 shows that ΔE_F increases about linearly with the band gap of the CIGSe layer. However, the distance to the Shockley–Queisser limited V_{oc}^{SQ} (ideal limit) also becomes larger. This indicates that bulk recombination increases with larger GGI. Nevertheless, a V_{oc} of 0.95 V should be possible based on the ΔE_F value of the $E_g = 1.5$ eV sample. While up to a band gap of 1.35 eV, the internal $\Delta E_F = E_{Fn} - E_{Fp}$ can be realized as external V_{oc}, above this value, additional effects must reduce the external V_{oc}. Together with the models presented above, we assign the difference between ΔE_F and the external V_{oc} for $E_g > 1.35$ eV to interface recombination limiting V_{oc} also for these RbF-treated MLU devices with CdS buffer layer. We emphasize that this happens even though the activation energy derived from $V_{oc}(T)$ approaches the band gap value (see Figure 15a).

6.5 | Na Concentration Adjustment by Na Precursor

In Figure 2b, it was shown that a higher substrate temperature increases the grain size of ClGSe layers with large GGI. Figure 17a on the other hand reveals that the Schott high-temperature glass releases less sodium into the MLU film than standard soda-lime glass. Hence, additional Na doping appears necessary. Motivated by the work of Pianezzi et al. for narrow-gap CIGSe [80], sequential NaF PDT and RbF PDT was tested. Figure 17b,c give V_{oc} and EQE data of MLU samples grown on soda-lime glass with different NaF PDT treatments (differentiated by the nominal NaF film thickness). It is obvious that V_{oc} and J_{sc}(from integrated EQE) monotonously

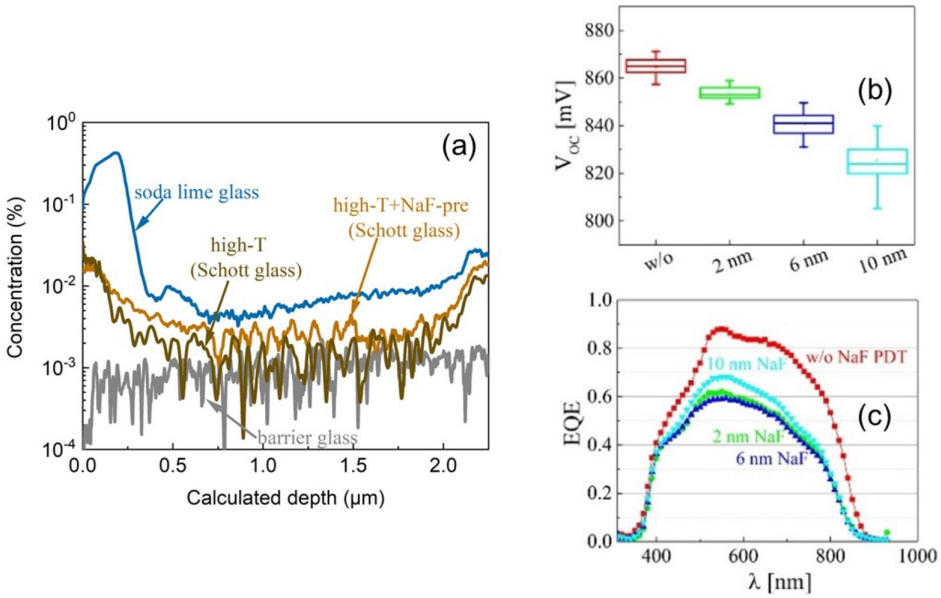

FIGURE 17 | (a) Quantified GDOES sodium concentration depth profiles for GGI = 0.75 MLU samples from 625°C process grown on soda-lime glass and on barrier glass as well as two high temperature 675°C processes on Schott glass with 8 nm NaF precursor layer and without NaF precursor. (b) V_{oc} of NaF + RbF PDT series where the NaF thickness was varied from 0 to 10 nm on standard soda-lime glass. (c) Respective EQE spectra from samples with different NaF PDT.

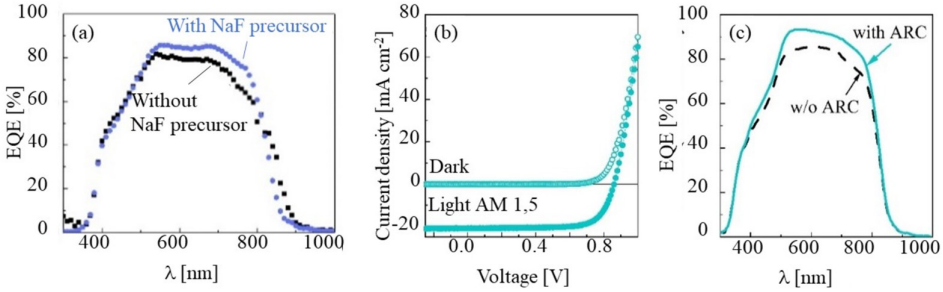

FIGURE 18 | CIGSe ($E_g = 1.48$ eV) devices on high temperature Schott glass and with 25 nm RbF-PDT. (a) EQE comparison of with and without 8 nm NaF precursor. (b) JV curves dark and illuminated after antireflection coating of device with NaF precursor and with optimized i-ZnO/ZnO:Al window as well as antireflection coating at ZSW. (c) EQE-signals of two devices with NaF precursor and optimized window with and without antireflection coating.

decline upon higher NaF thickness. Therefore, as an alternative, the application of a Na precursor was tested in combination with the high temperature glass. Figure 18a gives the EQE of a sodium precursor doped cell in comparison with a non-doped one. Both cells experienced a RbF PDT treatment. Comparing also with Figure 17c, a well-behaved EQE can be observed. Thus, a NaF precursor appears more appropriate for Na concentration adjustment on the high-temperature glass. Figure 18b,c show the JV curves and EQE of an optimized device (high-T glass, NaF precursor, RbF PDT) with optimized emitter stack [105]. With a band gap of 1.48 eV, this CIGSe cell exhibits $V_{oc} = 842\,\text{mV}$, $J_{sc} = 22.65\,\text{mA cm}^{-2}$, FF = 74.2%, and

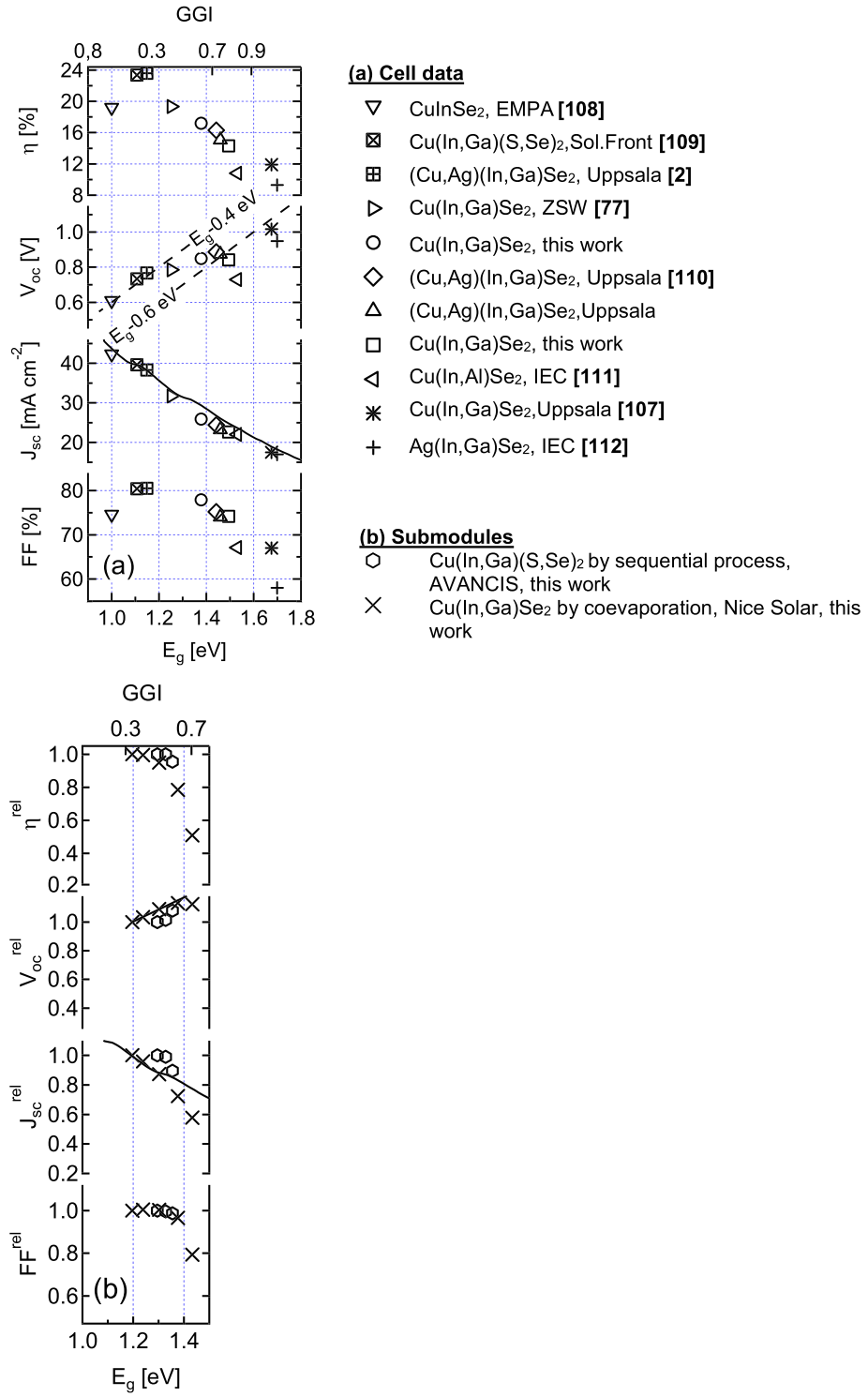

FIGURE 19 | Selection of normalized device parameters of (a) laboratory CIGSe cells as a function of band gap energy E_g (bottom axis) and GGI (top axis) from literature and own work. (b) Industrial pilot modules from CIGSe co-evaporation (NICE Solar—crosses) and sequential CIGSSe deposition (AVANCIS—hexagons). The V_{oc} trend line in (b) gives the relative change of the energy band gap calculated for $CuIn_{1-x}Ga_xSe_2$ with optical bowing parameter $b = 0.2$ (Table 4.12 in [49]). The J_{sc} trend line gives the relative change of the maximum possible short circuit current as a function of E_g (GGI).

$\eta = 14.15\%$ with antireflection coating. The diode quality factor was around 1.5. Inspecting the $V_{oc}(t)$ transient of this cell, it was found that it exhibits a negative slope ($\frac{dV_{oc}}{dt} < 0$) indicating the prevailing dominance of interface recombination.

6.6 | V_{oc} Exceeds the Absorber Built-In Potential Estimated From Theory

Solid state theory predicts a limitation of the absorber band bending at the junction for wide-gap CIGSe due to spontaneous Cu vacancy, V_{Cu}, formation [65]. If the Fermi energy moves up too high in the band gap, V_{Cu} vacancies are formed which lead to higher absorber p-type doping, thereby reducing and thus pinning the Fermi energy. This can also happen at the absorber surface where a strong band bending (high Fermi energy, i.e., large $E_{p,az=0}$ as in figure 2.24 of Ref. [49]) shall be the result of junction formation. Using photoelectron spectroscopy, Klein et al. observed a Fermi level pinning of $CuGaSe_2$ surfaces [75] at $E_F - E_v = 0.6$ Ev, which may impede the formation of a built-in potential in wide-gap CIGSe absorbers. Theoretical calculations using the LDA + U approach predicted a pinning position of $E_{p,a} = 0.6$ eV [65, 106]. Using hybrid functional calculations, a value of 0.8 eV was derived [19]. A limited $E_{p,a}$ would lead to strong interface recombination and hence would limit the V_{oc}. We ask here, if our results can support this model quantitatively, that is, using measured device values. Figure 14 shows that for a GGI above 0.8, a V_{oc} of 800 mV can be achieved. Employing a $Zn_{1-x}Sn_xO_y$ buffer layer (or electron transport layer) by atomic layer deposition, Larsson et al. even achieved above 1 V open-circuit voltage with an indium-free $CuGaSe_2$ absorber [107]. For a device which is limited by interface recombination, the saturation current comes out as $J_o = q\, N_{v,a}\, S_{p0}\, \exp\left\{ -\frac{E_{p,a_{z=0}}}{kT} \right\}$ where $N_{v,a}$ is the absorber valence band effective density of states, S_{p0} the hole recombination velocity, and $E_{p,az=0}$ is the distance between Fermi energy and valence band maximum at the absorber buffer interface $z = 0$. With this expression, we can determine $E_{p,a_{z=0}} = \frac{qV_{oc}}{A} + kTln\left(\frac{q\, N_{v,a}\, S_{p0}}{J_{sc}}\right)$. With $A = 1.5$ as realized in this work, $N_{v,a} = 1.5 \times 10^{19}\,cm^{-3}$, $J_{sc} = 22\,mA\,cm^{-2}$, $V_{oc} = 840$ mV, and an assumed $S_{p,0} = 10^3\,cm\,s^{-1}$ for the RbF-treated device, we calculate $E_{p,az=0} = 0.86$ eV. This value is already larger than the experimental pinning position and the theoretical predictions cited above.

6.7 | GGI in Industrial Processes Is Limited Below 0.4–0.5

Using industrial processes, the" increase of GGI has been tested by co-evaporated CIGSe (NICE Solar) and by sequential Cu (In,Ga)$(S,Se)_2$ (CIGSSe, AVANCIS) deposition. Figure 19a shows data for lab-scale CIGSe cells, while Figure 19b gives the normalized module data up to a GGI of 0.7 and compares with theoretical trend lines (see caption for more details). It is remarkable that J_{sc} of the modules in (b) decreases more strongly with an increasing band gap than for laboratory cells in (a). However, the module data also exhibit a decreasing FF. Above a certain GGI, the reduced J_{sc} is no longer compensated by enhanced V_{oc}. This threshold (GGI_{max}) is higher for the S-containing CIGSSe devices from a sequential Cu (In,Ga)$(S,Se)_2$ process ($GGI_{max} \approx 0.5$), than for the S-free CIGSe co-evaporation ($GGI_{max} \approx 0.4$).

7 | Conclusions

Physical, chemical, and electronic properties of Cu (In,Ga)Se_2 thin films with large gallium content (high GGI ratio) have been studied employing a variety of methods. It is found that the Ga gradient, which can impede carrier collection, can be reduced by three measures: Ga evaporation in the second stage of a three-stage process, increased substrate temperature, and sodium-free film growth. Also, the grain size can be increased by high-temperature glass as well as a sodium barrier, emphasizing that both promote chemical and grain-boundary diffusion. At high GGI, the CIGSe/CdS interface shows a pronounced cliff in the conduction band alignment, creating opportunities for interface recombination. Heavy alkali post-deposition treatments lead to clearly increased device performance, ascribed to *reduced* interface recombination. This is concluded from an increased activation energy of J_0, a reduced open-circuit voltage transient $V_{oc}(t)$, and from the small effect of heavy alkali doping on the time-resolved photoluminescence data. The reduced interface recombination could be due to an alkali-indium-selenium rich interface to the buffer layer, which may shift the absorber's valence band maximum away from E_F or which may reduce the interface state density. Using calibrated photoluminescence yield analysis, the impact of bulk and interface recombination in the device can be analyzed. Bulk recombination is higher than in narrow-gap CIGSe, perhaps partly due to the higher fraction of Cu-rich grain boundaries, as detected by APT. Above a GGI of 0.6, recombination at the CIGSe/CdS interface opens a gap between bulk quasi Fermi level splitting and the external open-circuit potential. Compared with laboratory cells, module technology employed in this work seems to allow a larger GGI increase without deteriorating the photovoltaic performance in particular upon adding sulfur to the absorber.

Author Contributions

Setareh Zahedi-Azad: writing, experiments, modelling. **Roland Scheer:** writing, review, editing, modelling, supervision, funding acquisition. **Dimitrios Hariskos**: investigation, data curation, writing – review and editing, visualization. **Stefan Paetel**: investigation, data curation, writing – review and editing, visualization. **Wolfram Hempel**: investigation, data curation, writing – review and editing, visualization. **Wolfram Witte**: investigation, data curation, writing – review and editing, visualization, project administration, funding acquisition. **Hao Luo**: data curation, formal analysis, investigation, methodology, software, writing – original draft. **Oana Cojocaru-Mirédin**: data curation, investigation, methodology, software, writing – review and editing, resources, funding acquisition, project administration. **Mary Blankenship**: investigation, formal analysis, visualization, writing-review and editing. **Dirk Hauschild**: conceptualization, investigation, formal analysis, visualization, supervision, writing – original draft. **Victor van Maris**: investigation, formal analysis, visualization, writing – review and editing. **Lothar Weinhardt**: conceptualization, formal analysis, supervision, funding acquisition, writing – review and editing. **Clemens Heske**: conceptualization, resources, formal analysis, supervision, funding acquisition, writing – review and editing. **Thomas Unold**: data curation, investigation, methodology, software, writing – review and editing, resources,

funding acquisition, project administration. **José A. Márquez**: curation, formal analysis, investigation, methodology, software, writing – original draft. **Jasmin Seeger**: method development, KPFM measurements and analysis. **Florian Wilhelmi**: method development, KPFM measurements and analysis. **Michael Hetterich**: project administration, methodology, data curation, investigation, writing – review and editing. **Thomas Niesen**: data curation, formal analysis, investigation, methodology, resources, writing – review and editing. **Patrick Eraerds**: funding acquisition, writing – review and editing. **Thomas Dalibor**: resources, writing – review and editing. **Xiaowei Jin**: FIB preparation of TEM samples, analytical and high-resolution TEM. **Reinhard Schneider**: coordination of TEM investigations, analysis of TEM data, supervision. **Dagmar Gerthsen**: writing – review and editing, supervision, funding acquisition, project administration. **Di Wang**: resources. **Christian Kübel**: supervision, funding acquisition.

Acknowledgements

This work was funded by the German Federal Ministry for Economic Affairs and Energy (BMWi) under contract number 0324076A-0324076F within the EFFCIS project and by the German Federal Ministry for Economic Affairs and Climate Action (BMWK) under contract number 03EE1059A-03EE1059E within the EFFCIS-II project. The authors thank the colleagues from NICE Solar and Schott AG for providing samples. Open Access funding enabled and organized by Projekt DEAL.

Data Availability Statement

The data that support the findings of this study are available from the corresponding author upon reasonable request.

Endnotes

[1] The melting point of $CuInSe_2$ is 1260 K, while that of $CuGaSe_2$ is 1310–1340 K [52] Landolt, Börnstein, in: A. Goldmann, E.E. Koch (Eds.), Numerical data and functional relationships in science and technology, Springer, Berlin, 1989.

[2] Scanning TEM High-Angle Annular Dark-Field Imaging

References

1. S. Ishizuka, "CuGaSe2 Thin Film Solar Cells: Challenges for Developing Highly Efficient Wide-Gap Chalcopyrite Photovoltaics," *Physica Status Solidi A-Applied Research* 216, no. 15 (2019): 1800873.

2. J. Keller, K. Kiselman, O. Donzel-Gargand, et al., "High-Concentration Silver Alloying and Steep Back-Contact Gallium Grading Enabling Copper Indium Gallium Selenide Solar Cell with 23.6% Efficiency," *Nature Energy* 9, no. 4 (2024): 467–478.

3. L. Weinhardt, D. G. O. Fuchs, G. Storch, et al., "Band Alignment at the CdS/Cu (In,Ga)S_2 Interface in Thin-Film Solar Cells," *Applied Physics Letters* 86 (2005): 062109.

4. M. Blankenship, D. Hauschild, L. Both, et al., "Conduction Band Cliff at the CdS/CuIn0.1Ga0.9Se2 Thin-Film Solar Cell Interface," *Journal of Physical Chemistry C* 128, no. 1 (2024): 339–345.

5. R. Scheer and H. Wilhelm, "Efficiency Limitation of Chalcopyrite and Kesterite Solar Cells," in *Proceedings 37th IEEE Photovoltaic Specialists Conference* (IEEE, 2011), 2500.

6. F. Obereigner, N. Barreau, W. Witte, and R. Scheer, "Open-Circuit and Doping Transients of Cu (In,Ga)Se2 Solar Cells With Varying Ga Content," *Journal of Applied Physics* 117, no. 5 (2015): 055774.

7. M. Morkel, L. Weinhardt, B. Lohmüller, et al., "Flat Conduction Band Alignment at the CdS/CuInSe$_2$ Thin-Film Solar Cell Heterojunction," *Applied Physics Letters* 79, no. 27 (2001): 4482–4484.

8. L. Weinhardt, C. Heske, E. Umbach, T. P. Niesen, S. Visbeck, and F. Karg, "Band Alignment at the i-ZnO/CdS Interface in Cu (In,Ga)$(S,Se)_2$ Thin-Film Solar Cells," *Applied Physics Letters* 84, no. 16 (2004): 3175–3177.

9. M. Mezher, R. Garris, L. M. Mansfield, et al., "Electronic Structure of the Zn(O,S)/Cu(In,Ga)Se2 Thin-Film Solar Cell Interface," *Progress in Photovoltaics: Research and Applications* 24, no. 8 (2016): 1142–1148.

10. D. Hauschild, D. Kreikemeyer-Lorenzo, P. Jackson, et al., "Impact of a RbF Postdeposition Treatment on the Electronic Structure of the CdS/Cu (In,Ga)Se2 Heterojunction in High-Efficiency Thin-Film Solar Cells," *ACS Energy Letters* 2, no. 10 (2017): 2383–2387.

11. D. Hauschild, F. Meyer, A. Benkert, et al., "Improving Performance by Na Doping of a Buffer Layer—Chemical and Electronic Structure of the InxSy:Na/CuIn(S,Se)2 Thin-Film Solar Cell Interface," *Progress in Photovoltaics: Research and Applications* 26, no. 5 (2018): 359–366.

12. L. Weinhardt, D. Hauschild, and C. Heske, "Surface and Interface Properties in Thin-Film Solar Cells: Using Soft X-Rays and Electrons to Unravel the Electronic and Chemical Structure," *Advanced Materials* 31, no. 26 (2019): 1806660.

13. N. Terada, R. T. Widodo, K. Itoh, et al., "Characterization of Interface Nature and Band Alignment in CBD-CdS/Cu (In,Ga)Se2 Bi-Layer Structure by Photoemission and Inverse Photoemission Spectroscopy," *Thin Solid Films* 480-481 (2005): 183–187.

14. H. Kashiwabara, Y. Hayase, K. Takeshita, et al., "Study of Changes of Electronic and Structural Nature of CBD-CDS/CIGS Interface With Ga Concentration," in *2006 IEEE 4th World Conference on Photovoltaic Energy Conference* (IEEE, 2006), 495–498.

15. F. Larsson, N. S. Nilsson, J. Keller, et al., "Record 1.0 V Open-Circuit Voltage in Wide Band Gap Chalcopyrite Solar Cells," *Progress in Photovoltaics: Research and Applications* 25, no. 9 (2017): 755–763.

16. S. Ishizuka, J. Nishinaga, Y. Kamikawa, T. Nishida, and P. J. Fons, "Photovoltaic Efficiency Enhancement of Indium-Free Wide-Bandgap Chalcopyrite Solar Cells via an Aluminum-Induced Back-Surface Field Effect," *ACS Applied Materials & Interfaces* 17, no. 2 (2025): 3136–3145.

17. R. Scheer, "Activation Energy of Heterojunction Diode Currents in the Limit of Interface Recombination," *Journal of Applied Physics* 105 (2009): 104505.

18. A. Klein and W. Jaegermann, "Fermi Level Dependent Defect Formation in Cu-Chalcopyrite Semiconductors," *Applied Physics Letters* 74 (1999): 2283–2285.

19. J. Pohl and K. Albe, "Intrinsic Point Defects in $CuInSe_2$ and $CuGaSe_2$ as Seen via Screened-Exchange Hybrid Density Functional Theory," *Physical Review. B, Condensed Matter* 87, no. 24 (2013): 245203.

20. S. Zahedi-Azad and R. Scheer, "Quenching Interface Recombination in Wide Bandgap Cu (In,Ga)Se2 by Potassium Treatment," *Physica Status Solidi C, Current Topics in Solid State Physics* 14, no. 6 (2017): 1600203.

21. M. Raghuwanshi, E. Cadel, P. Pareige, et al., "Influence of Grain Boundary Modification on Limited Performance of Wide Bandgap Cu (In,Ga)Se2 Solar Cells," *Applied Physics Letters* 105, no. 1 (2014): 013902.

22. P. Tsoulka, A. Rivalland, L. Arzel, and N. Barreau, "Improved CuGaSe2 Absorber Properties Through a Modified Co-Evaporation Process," *Thin Solid Films* 709 (2020): 138224.

23. P. Jackson, R. Wuerz, D. Hariskos, E. Lotter, W. Witte, and M. Powalla, "Effects of Heavy Alkali Elements in Cu (In,Ga)Se2 Solar Cells With Efficiencies up to 22.6%," *physica status solidi (RRL) – Rapid Research Letters* 10, no. 8 (2016): 583–586.

24. S. Siebentritt, E. Avancini, M. Bär, et al., "Heavy Alkali Treatment of Cu (In,Ga)Se2 Solar Cells: Surface Versus Bulk Effects," *Advanced Energy Materials* 10, no. 8 (2020): 1903752.

25. S. Ishizuka, N. Taguchi, J. Nishinaga, Y. Kamikawa, S. Tanaka, and H. Shibata, "Group III Elemental Composition Dependence of RbF Postdeposition Treatment Effects on Cu (In,Ga)Se2 Thin Films and Solar Cells," *Journal of Physical Chemistry C* 122, no. 7 (2018): 3809–3817.

26. N. Taguchi, S. Tanaka, and S. Ishizuka, "Direct Insights into RbInSe2 Formation at Cu (In,Ga)Se2 Thin Film Surface With RbF Postdeposition Treatment," *Applied Physics Letters* 113, no. 11 (2018): 113903.

27. A. Nikolaeva, M. Krause, N. Schäfer, et al., "Electrostatic Potential Fluctuations and Light-Soaking Effects in Cu (In,Ga)Se2 Solar Cells," *Progress in Photovoltaics: Research and Applications* 28, no. 9 (2020): 919–934.

28. S. Ishizuka, A. Yamada, P. J. Fons, H. Shibata, and S. Niki, "Structural Tuning of Wide-Gap Chalcopyrite CuGaSe2 Thin Films and Highly Efficient Solar Cells: Differences from Narrow-Gap Cu (In,Ga)Se2," *Progress in Photovoltaics: Research and Applications* 22, no. 7 (2014): 821–829.

29. J. Keller, K. V. Sopiha, O. Stolt, et al., "Wide-Gap (Ag,Cu)(In,Ga)Se2 Solar Cells with Different Buffer Materials—A Path to a Better Heterojunction," *Progress in Photovoltaics Research and Applications* 28, no. 4 (2020): 237–250.

30. K. Kim, S. K. Ahn, J. H. Choi, et al., "Highly Efficient Ag-alloyed Cu (In,Ga)Se2 Solar Cells with Wide Bandgaps and Their Application to Chalcopyrite-based Tandem Solar Cells," *Nano Energy* 48 (2018): 345–352.

31. P. Pearson, J. Keller, L. Stolt, O. Donzel-Gargand, and C. Platzer Björkman, "Ag-Dependent Behavior Threshold and Metastability in Wide-Gap (Ag,Cu)(In,Ga)Se2 Solar Cells," *Solar RRL* 8, no. 11 (2024): 2400220.

32. S. Zahedi-Azad, E. Jarzembowski, S. Hartnauer, L. Wägele, D. Greiner, and R. Scheer, "Monitoring the Phase Evolution of Cu (In,Ga)Se2 by Different Se Flux via In-situ XRD," *physica status solidi (a)* 213, no. 8 (2016): 2169–2175.

33. G. Voorwinden, R. Kniese, and M. Powalla, "In-Line Cu (In,Ga)Se2 Co-Evaporation Processes With Graded Band Gaps on Large Substrates," *Thin Solid Films* 431-432 (2003): 538–542.

34. M. Algasinger, T. Niesen, T. Dalibor, et al., "Efficient Cu (In,Ga)(Se,S)2 Modules With Sputtered Zn(O,S) Buffer Layer," *Thin Solid Films* 633 (2017): 231–234.

35. C. Schubbert, P. Eraerds, M. Richter, et al., "Performance Ratio Study Based on a Device Simulation of a 2D Monolithic Interconnected Cu (In,Ga)(Se,S)2 Solar Cell," *Solar Energy Materials and Solar Cells* 157 (2016): 146–153.

36. J. Seeger, F. Wilhelmi, J. Schundelmeier, et al., "Cross-Sectional Kelvin Probe Force Microscopy on Cu (In,Ga)Se2 Solar Cells: Influence of RbF and KF Post-Deposition Treatment on the Surface Potential of the Absorber Layer," *Applied Physics Letters* 117, no. 24 (2020): 201–212.

37. B. Gault, A. Chiaramonti, O. Cojocaru-Mirédin, et al., "Atom Probe Tomography," *Nature Reviews Methods Primers* 1, no. 1 (2021): 51.

38. O. Cojocaru-Mirédin, T. Schwarz, and D. Abou-Ras, "Assessment of Elemental Distributions at Line and Planar Defects in Cu (In,Ga)Se2 Thin Films by Atom Probe Tomography," *Scripta Materialia* 148 (2018): 106–114.

39. O. Cojocaru-Mirédin, T. Schwarz, P. P. Choi, M. Herbig, R. Wuerz, and D. Raabe, "Atom Probe Tomography Studies on the Cu (In,Ga)Se_2 Grain Boundaries," *Journal of Visualized Experiments* 74 (2013): e50376.

40. O. Cojocaru-Mirédin, P. P. Choi, D. Abou-Ras, S. S. Schmidt, R. Caballero, and D. Raabe, "Characterization of Grain Boundaries in Cu (In,Ga)Se_2 Films Using Atom-Probe Tomography," *IEEE Journal of Photovoltaics* 1, no. 2 (2011): 207–212.

41. H. Kempa, T. Rissom, U. Hlawatsch, et al., "Metastability of Solar Cells Based on Evaporated Chalcopyrite Absorber Layers Prepared With Varying Selenium Flux," *Thin Solid Films* 535 (2013): 340–342.

42. J. Moulder, W. Stickle, W. Sobol, and K. D. Bomben, *Handbook of X-Ray Photoelectron Spectroscopy* (Eden Prairie, MN: Perkin-Elmer Corporation, 1992).

43. T. Orgis, M. Maiberg, and R. Scheer, "Influence of Band Gradients on CIGS Solar Cell Diode Factors," *Journal of Applied Physics* 114 (2013): 214506.

44. M. Krause, A. Nikolaeva, M. Maiberg, et al., "Microscopic Origins of Performance Losses in Highly Efficient Cu (In,Ga)Se2 Thin-Film Solar Cells," *Nature Communications* 11, no. 1 (2020): 4189.

45. S. Zahedi-Azad, M. Maiberg, and R. Scheer, "Effect of Na-PDT and KF-PDT on the Photovoltaic Performance of Wide Bandgap Cu (In,Ga)Se2 Solar Cells," *Progress in Photovoltaics, Research and Applications* 28, no. 11 (2020): 1146–1157.

46. W. Witte, D. Abou-Ras, K. Albe, et al., "Gallium Gradients in Cu (In,Ga)Se2 Thin-Film Solar Cells," *Progress in Photovoltaics: Research and Applications* 23, no. 6 (2015): 717–733.

47. H. Rodriguez-Alvarez, R. Mainz, and S. Sadewasser, "A One-Dimensional Fickian Model to Predict the Ga Depth Profiles in Three-Stage Cu (In,Ga)Se2," *Journal of Applied Physics* 115, no. 20 (2014): 204913.

48. V. Nadenau, D. Hariskos, H.-W. Schock, et al., "Microstructural Study of the CdS/$CuGaSe_2$ Interfacial Region in $CuGaSe_2$ Thin Film Solar Cells," *Journal of Applied Physics* 85, no. 1 (1999): 534–542.

49. R. Scheer and H.-W. Schock, *Chalcogenide Photovoltaics—Physics, Technologies, and Thin Film Devices* (Weinheim: Wiley VCH, 2011).

50. M. Ishii, K. Shibata, and H. Nozaki, "Anion Distributions and Phase Transitions in $CuS_{1-x}Se_x$(x=0-1) Studied by Raman Spectroscopy," *Journal of Solid State Chemistry* 105 (1993): 504–511.

51. M. A. Contreras, L. M. Mansfield, B. Egaas, et al., "Wide Bandgap Cu (In,Ga)Se_2 Solar Cells With Improved Energy Conversion Efficiency," *Progress in Photovoltaics: Research and Applications* 20 (2012): 843–850.

52. Landolt, Börnstein, *Numerical Data and Functional Relationships in Science and Technology*, eds. A. Goldmann and E. E. Koch (Berlin: Springer, 1989).

53. M. Marudachalam, R. W. Birkmire, H. Hichri, J. M. Schultz, A. Swartzlander, and M. M. Al-Jassim, "Phases, Morphology, and Diffusion in $CuIn_xGa_{1-x}Se_2$ Thin Films," *Journal of Applied Physics* 82, no. 6 (1997): 2896–2905.

54. M. N. Ruberto and A. Rothwarf, "Time-Dependent Open Circuit Voltage in $CuInSe_2$/CdS Solar Cells: Theory and Experiment," *Journal of Applied Physics* 61, no. 9 (1987): 4662–4669.

55. T. Meyer, M. Schmidt, F. Engelhardt, J. Parisi, and U. Rau, "A Model for the Open Circuit Voltage Relaxation in Cu (In,Ga)Se_2 Heterojunction Solar Cells," *European Physical Journal Applied Physics* 8 (1999): 43–52.

56. T. Hölscher, S. Förster, T. Schneider, M. Maiberg, W. Widdra, and R. Scheer, "Light Induced Degradation of Cu (In,Ga)Se2 Thin Film Surfaces," *Applied Physics Letters* 111, no. 1 (2017): 011604.

57. M. Maiberg and R. Scheer, "Theoretical Study of Time-Resolved Luminescence in Semiconductor Heterostructures. 2. Pulsed Excitation," *Journal of Applied Physics* 116 (2014): 123711.

58. M. Maiberg, T. Hölscher, S. Zahedi-Azad, W. Fränzel, and R. Scheer, "Investigation of Long Lifetimes in Cu (In,Ga)Se2 by Time-Resolved Photoluminescence," *Applied Physics Letters* 107, no. 12 (2015): 122104.

59. M. Maiberg, T. Hölscher, S. Zahedi-Azad, and R. Scheer, "Theoretical Study of Time-Resolved Luminescence in Semiconductors. 3. Trap States in the Band Gap," *Journal of Applied Physics* 118 (2015): 105701.

60. A. Karami, M. Morawski, H. Kempa, R. Scheer, and O. Cojocaru-Mirédin, "Sodium in Cu (In, Ga)Se2 Solar Cells: To Be or Not to Be Beneficial," *Solar RRL* 8, no. 3 (2024): 2300544.

61. Kodalle T. Unraveling the Structural and Optoelectronic Effects of Rb on Chalcopyrite Solar Cells, Martin-Luther-Universität Halle/Wittenberg 2020.

62. Zahedi-Azad, S., M. Maiberg, R. Clausing, and R. Scheer, "Influence of Heavy Alkali Post Deposition Treatment on Wide Gap Cu (In,Ga) Se2," *Thin Solid Films* 669 (2019): 629–632.

63. C. Heske, D. Eich, R. Fink, et al., "Observation of Intermixing at the Buried CdS/CuInGaSe2 Thin Film Solar Cell Heterojunction," *Applied Physics Letters* 74, no. 10 (1999): 1451–1453.

64. L. Weinhardt, M. Bär, S. Pookpanratana, et al., "Sulfur Gradient-Driven Se Diffusion at the CdS/CuIn(S,Se)2 Solar Cell Interface," *Applied Physics Letters* 96, no. 18 (2010): 182102.

65. S. B. Zhang, S.-H. Wei, and A. Zunger, "A Phenomenological Model for Systematization and Prediction of Doping Limits in II-VI and I-III-VI2 Compounds," *Journal of Applied Physics* 83, no. 6 (1998): 3192–3196.

66. E. Ghorbani, P. Erhart, and K. Albe, "Energy Level Alignment of Cu (In, Ga) (S, se)$_2$ Absorber Compounds With In_2S_3, $NaIn_5S_8$, and $CuIn_5S_8$ cd-Free Buffer Materials," *Physical Review Materials* 3, no. 7 (2019): 075401.

67. C. Persson, C. Platzer-Björkman, J. Malmström, T. Törndahl, and M. Edoff, "Strong Valence-Band Offset Bowing of ZnO1-xSx Enhances p-Type Nitrogen Doping of ZnO-Like Alloys," *Physical Review Letters* 97, no. 14 (2006): 146403.

68. J. J. Yeh and I. Lindau, "Atomic Subshell Photoionization Cross Sections and Asymmetry Parameters: 1Z103," *Atomic Data and Nuclear Data Tables* 32, no. 1 (1985): 1–155.

69. A. Naumkin, A. Kraut-Vass, S. Gaarenstroom, and C. Powell, NIST X-Ray Photoelectron Spectroscopy (XPS) Database, Version 4.1, http://srdata.nist.gov/xps/Default.aspx, 2000.

70. E. Handick, P. Reinhard, R. G. Wilks, et al., "Formation of a K—In—Se Surface Species by NaF/KF Postdeposition Treatment of Cu (In,Ga)Se2 Thin-Film Solar Cell Absorbers," *ACS Applied Materials & Interfaces* 9, no. 4 (2017): 3581–3589.

71. D. Schmid, M. Ruckh, and H. W. Schock, "Photoemission Studies on Cu (In,Ga)Se2 Thin Films and Related Binary Selenides," *Applied Surface Science* 103 (1996): 409–429.

72. T. Gleim, C. Heske, E. Umbach, et al., "Formation of the ZnSe/(Te/)GaAs(100) Heterojunction," *Surface Science* 531, no. 1 (2003): 77–85.

73. T. Gleim, C. Heske, E. Umbach, et al., "Reduction of the ZnSe/GaAs(100) Valence Band Offset by a Te Interlayer," *Applied Physics Letters* 78, no. 13 (2001): 1867–1869.

74. B. Dimmler, F. Grunwald, D. Schmid, and H. W. Schock, "Analysis of UHV Prepared CIS Films With Surface and Bulk Sensitive Methods," in *22nd IEEE Photovoltaic Specialists Conference* (New York, Las Vegas: IEEE, 1991), 1088.

75. A. Klein, J. Fritsche, W. Jaegermann, J. H. Schön, C. Kloc, and E. Bucher, "Fermi Level-Dependent Defect Formation at Cu (In,Ga)Se_2 Interfaces," *Applied Surface Science* 166, no. 1–4 (2000): 508–512.

76. Y.-J. Zhao, C. Persson, S. Lany, and A. Zunger, "Why can $CuInSe_2$ Be Readily Equilibrium-Doped n-Type but the Wider-Gap $CuGaSe_2$ Cannot?," *Applied Physics Letters* 85 (2004): 5860–5862.

77. P. Jackson, D. Hariskos, R. Wuerz, W. Wischmann, and M. Powalla, "Compositional Investigation of Potassium Doped Cu (In,Ga)Se2 Solar Cells With Efficiencies up to 20.8%," *Physica Status Solidi (RRL) – Rapid Research Letters* 8, no. 3 (2014): 219–222.

78. T. Kodalle, R. Kormath Madam Raghupathy, T. Bertram, et al., "Properties of Co-Evaporated RbInSe2 Thin Films," *Physica Status Solidi (RRL) – Rapid Research Letters* 13, no. 3 (2019): 1800564.

79. T. P. Weiss, S. Nishiwaki, B. Bissig, et al., "Injection Current Barrier Formation for RbF Postdeposition-Treated Cu (In,Ga)Se2-Based Solar Cells," *Advanced Materials Interfaces* 5, no. 4 (2018): 1701007.

80. F. Pianezzi, P. Reinhard, A. Chirilă, et al., "Unveiling the Effects of Post-Deposition Treatment With Different Alkaline Elements on the Electronic Properties of CIGS Thin Film Solar Cells," *Physical Chemistry Chemical Physics* 16, no. 19 (2014): 8843–8851.

81. E. Handick, P. Reinhard, J.-H. Alsmeier, et al., "Potassium Postdeposition Treatment-Induced Band Gap Widening at Cu (In, Ga) Se_2 Surfaces–Reason for Performance Leap?," *ACS Applied Materials & Interfaces* 7 (2015): 27414.

82. Z. Z. Kish, E. Y. Peresh, V. B. Lazarev, and E. E. Semrad, "Systematics and the Rules of Variations in the Properties of the AIBIIIC2VI-Type Compounds Izvestiia Akademii Nauk SSSR," *Neorganicheskie Materialy* 23 (1987): 777.

83. J. Weis, H. D. Schäfer, and G. Schön, "Neue ternäre Telluride und Selenide der Alkalimetalle mit Elementen der 3. Hauptgruppe," *Zeitschrift Für Naturforschung. B, Chemical Sciences* 31 (1976): 1336–1340.

84. H. Luo, A. Karami, H. Mirhosseini, R. Wuerz, W. Witte, O. Cojucaru-Miredin, in preparation.

85. F. Q. Huang, B. Deng, D. E. Ellis, and J. A. Ibers, "Preparation, Structures, and Band Gaps of RbInS2 and RbInSe2," *Journal of Solid State Chemistry* 178, no. 6 (2005): 2128–2132.

86. T. Lepetit, S. Harel, L. Arzel, G. Ouvrard, and N. Barreau, "KF Post Deposition Treatment in Co-Evaporated Cu (In,Ga)Se2 Thin Film Solar Cells: Beneficial or Detrimental Effect Induced by the Absorber Characteristics," *Progress in Photovoltaics: Research and Applications* 25, no. 12 (2017): 1068–1076.

87. T. Kodalle, L. Choubrac, L. Arzel, R. Schlatmann, N. Barreau, and C. A. Kaufmann, "Effects of KF and RbF Post Deposition Treatments on the Growth of the CdS Buffer Layer on CIGS Thin Films—a Comparative Study," *Solar Energy Materials and Solar Cells* 200 (2019): 109997.

88. T. Kodalle, *Unraveling the Structural and Optoelectronic Effects of Rb on Chalcopyrite Solar Cells, Naturwissenschaftliche Fakultät II* (Martin-Luther-Universität Halle-Wittenberg, 2020).

89. M. Raghuwanshi, M. Chugh, G. Sozzi, et al., "Fingerprints Indicating Superior Properties of Internal Interfaces in Cu (In,Ga) Se2 Thin-Film Solar Cells," *Advanced Materials* 34, no. 37 (2022): 2203954.

90. P. Schöppe, S. Schönherr, R. Wuerz, et al., "Rubidium Segregation at Random Grain Boundaries in Cu (In,Ga)Se2 Absorbers," *Nano Energy* 42 (2017): 307–313.

91. P. Schöppe, S. Schönherr, M. Chugh, et al., "Revealing the Origin of the Beneficial Effect of Cesium in Highly Efficient Cu (In,Ga)Se2 Solar Cells," *Nano Energy* 71 (2020): 104622.

92. D. Abou-Ras, A. Nikolaeva, S. Caicedo Dávila, et al., "No Evidence for Passivation Effects of Na and K at Grain Boundaries in Polycrystalline Cu (In,Ga)Se2 Thin Films for Solar Cells," *Solar RRL* 3, no. 8 (2019): 1900095.

93. N. Nicoara, R. Manaligod, P. Jackson, et al., "Direct Evidence for Grain Boundary Passivation in Cu (In,Ga)Se2 Solar Cells Through Alkali-Fluoride Post-Deposition Treatments," *Nature Communications* 10, no. 1 (2019): 3980.

94. I. L. Eisgruber, J. E. Granata, J. R. Sites, J. Hou, and J. Kessler, "Blue-Photon Modification of Nonstandard Diode Barrier in $CuInSe_2$ Solar Cells," *Solar Energy Materials and Solar Cells* 53 (1998): 367–377.

95. A. Niemegeers, M. Burgelman, R. Herberholz, U. Rau, D. Hariskos, and H.-W. Schock, "Model for Electronic Transport in Cu (In,Ga)Se_2 Solar Cells," *Progress in Photovoltaics Research and Applications* 6 (1998): 407–421.

96. T. Eisenbarth, T. Unold, R. Caballero, C. A. Kaufmann, and H.-W. Schock, "Interpretation of Admittance, Capacitance-Voltage, and Current-Voltage Signatures in Cu (In,Ga)Se[sub 2] Thin Film Solar Cells," *Journal of Applied Physics* 107, no. 3 (2010): 034509.

97. T. Ott, F. Schönberger, T. Walter, et al., "Verification of Phototransistor Model for Cu (In,Ga)Se2 Solar Cells," *Thin Solid Films* 582 (2015): 392–396.

98. T. Schneider, C. Dethloff, T. Hölscher, H. Kempa, and R. Scheer, "Comparison of Mo and ITO Back Contacts in CIGSe Solar Cells: Vanishing of the Main Capacitance Step," *Progress in Photovoltaics: Research and Applications* 30, no. 2 (2022): 191–202.

99. H. Tangara, S. Zahedi-Azad, J. Not, et al., "Study of Defect Properties and Recombination Mechanism in Rubidium Treated cu (In, Ga)Se2 Solar Cells," *Journal of Applied Physics* 129, no. 18 (2021): 183108.

100. F. Pianezzi, P. Reinhard, A. Chirilă, et al., "Defect Formation in Cu (In,Ga)Se2 Thin Films Due to the Presence of Potassium During Growth by Low Temperature Co-Evaporation Process," *Journal of Applied Physics* 114, no. 19 (2013): 194508.

101. S. Siebentritt, "Wide gap Chalcopyrites: Material Properties and Solar Cells," *Thin Solid Films* 403-404 (2002): 1–8.

102. H. Wilhelm, H.-W. Schock, and R. Scheer, "Interface Recombination in Heterojunction Solar Cells: Influence of Buffer Layer Thickness," *Journal of Applied Physics* 109 (2011): 084514.

103. M. S. Lyam, T. Hölscher, M. Maiberg, et al., "Dominant Recombination Path in Low-Bandgap Kesterite CZTSe(S) Solar Cells From Red Light Induced Metastability," *Journal of Applied Physics* 129, no. 20 (2021): 205703.

104. T. Unold and L. Gütay, *Advanced Characterization Techniques for Thin Film Solar Cells*, eds. D. Abou-Ras, T. Kirchartz, and U. Rau (WILEY-VCH Verlag GmbH & Co. KGaA, 2011).

105. P. Jackson, D. Hariskos, E. Lotter, et al., "New World Record Efficiency for Cu (In,Ga)Se_2 Solar Cells Beyond 20%," *Progress in Photovoltaics Research and Applications* 17 (2011): 894.

106. B. Himmetoglu, A. Floris, S. de Gironcoli, and M. Cococcioni, "Hubbard-Corrected DFT Energy Functionals: The LDA+U Description of Correlated Systems," *International Journal of Quantum Chemistry* 114, no. 1 (2014): 14–49.

107. F. Larsson, N. S. Nilsson, J. Keller, et al., "Record 1.0 V Open-Circuit Voltage in Wide Band Gap Chalcopyrite Solar Cells," *Progress in Photovoltaics* 25, no. 9 (2017): 755–763.

108. T. Feurer, R. Carron, G. Torres Sevilla, et al., "Efficiency Improvement of Near-Stoichiometric CuInSe2 Solar Cells for Application in Tandem Devices," *Advanced Energy Materials* 9, no. 35 (2019): 1901428.

109. M. A. Green, E. D. Dunlop, D. H. Levi, J. Hohl-Ebinger, M. Yoshita, and A. W. Y. Ho-Baillie, "Solar Cell Efficiency Tables (Version 54)," *Progress in Photovoltaics: Research and Applications* 27, no. 7 (2019): 565–575.

110. J. Keller, H. Aboulfadl, L. Stolt, O. Donzel-Gargand, and M. Edoff, "Rubidium Fluoride Absorber Treatment for Wide-Gap (Ag,Cu)(In,Ga)Se2 Solar Cells," *Solar RRL* 6, no. 6 (2022): 2200044.

111. P. D. Paulson, M. W. Haimbodi, S. Marsillac, R. Birkmire, and W. N. Shafarman, "$CuIn_{1-x}Al_xSe_2$ Thin Films and Solar Cells," *Journal of Applied Physics* 91, no. 12 (2002): 10153–10156.

112. G. M. Hanket, J. H. Boyle, and W. N. Shafarman, "Characterization and Device Performance of (Ag,Cu)(In,Ga)Se2 Absorber Layers, Proceedings," in *34th IEEE Photovoltaic Specialists Conference* (IEEE, 2009), 1240.

Supporting Information

Additional supporting information can be found online in the Supporting Information section. **Figure S1:** Capacitance-frequency curves of RbF-treated and untreated MLU CIGSe samples in the relaxed state and after 15, 45, and 120 min of light soaking, samples with (a) GGI = 0.30 and (b) GGI = 0.75. **Figure S2:** Raman spectra of Cu (In,Ga)(Se,S)2 absorbers prepared by the sequential process of AVANCIS with GGI = 0.55 and 0.59. **Figure S3:** Surface potential difference and derived CIGSe work function ΦCIGSe for CIGSe cross-sections with different GGI and PDT treatments. Data replotted from Ref. [37].